



# Buckling behavior of multilayer cylindrical shells composed of functionally graded nanocomposite layers under lateral pressure in thermal environments

M. Avey<sup>a,b,c</sup>, N. Fantuzzi<sup>d</sup>, A.H. Sofiyev<sup>e,f,g,\*</sup>, A.D. Zamanov<sup>h</sup>, Y.N. Hasanov<sup>i</sup>, E. Schnack<sup>j</sup>

<sup>a</sup> Department of Mathematical Engineering, Graduate School of Istanbul Technical University, 34469 Maslak, Istanbul, Turkey

<sup>b</sup> Analytical Information Resources Center of UNEC-Azerbaijan State Economics University, 1001 Baku, Azerbaijan

<sup>c</sup> Application and Research Center, Istanbul Ticaret University, 34445 Istanbul, Turkey

<sup>d</sup> Department of Civil, Chemical, Environmental, and Materials Engineering, University Bologna, 40136 Bologna, Italy

<sup>e</sup> Department of Mathematics, Istanbul Ticaret University, Beyoglu, 34445 Istanbul, Turkey

<sup>f</sup> Scientific Research Centers for Composition Materials of UNEC Azerbaijan State Economic University, Baku 100 Azerbaijan

<sup>g</sup> Scientific Research Department of Azerbaijan University of Architecture and Construction, Baku 1073, Azerbaijan

<sup>h</sup> Department of Mathematical Analysis, Azerbaijan State Pedagogical University, 1000 Baku, Azerbaijan

<sup>i</sup> Department of Applied Mechanics Azerbaijan State Marine Academy, Baku, Azerbaijan

<sup>j</sup> Department of Solids Mechanics, Karlsruhe Institute of Technology, Karlsruhe, Germany

## ARTICLE INFO

### Keywords:

Multilayer cylindrical shells  
Functionally graded carbon nanotube-patterned layers  
Thermal effect  
Lateral critical pressure  
Shear deformation theory

## ABSTRACT

In this study, the stability behavior of multilayer cylindrical shells made of functionally graded nanocomposite layers (FG-NCLs) subjected to the lateral pressure in thermal environments is investigated. It is postulated that nanocomposite layers forming layered cylindrical shells are made of single-walled carbon nanotube (SWCNT)-reinforced polymers that have four types of profiles based on the uniform and linear distributions of mechanical properties. The material properties of SWCNTs are assumed to be dependent on location as well as temperature and are obtained from molecular dynamics simulations. The governing equations are derived as partial differential equations within shear deformation theory (SDT) and solved in a closed form, using the Galerkin procedure, to determine the lateral critical pressure (LCP) in thermal environments. The numerical representations relate to the buckling behavior of multilayer cylindrical shells made of functionally graded nanocomposite layers under the uniform lateral pressure for different CNT patterns and temperatures within SDT and Kirchhoff-Love theory (KLT).

## 1. Introduction

The exceptional properties of carbon nanotubes (CNTs) such as high modulus of elasticity, high tensile strength and stiffness make it the most attractive type of reinforcement for the formation of nanocomposites besides using it as the main structural element [1–3]. The nanocomposites obtained by reinforcing CNTs to the metal, ceramic or polymer matrices are increasingly used in various fields of the modern technology. The nanocomposites are materials that offer many advantages to producers and consumers such as improved properties, less solid waste and modern production techniques. According to the application percentages of the ceramic, metal and polymer-based nanocomposites, polymer-based nanocomposites are the most preferred. In addition, the

nanocomposites exhibit significantly improved mechanical, thermal, optical and physicochemical properties compared to pure polymers. Similarly, in nanocomposites, thermal stability, non-flammability, physical, mechanical and barrier properties are much better than conventional composite systems. The extensive research on the properties of polymer-based carbon nanotube reinforced composites (CNTRCs) reveals that even at very low volume fractions, reinforcement of CNTs improves the mechanical and thermal properties of the polymer matrix [4–9].

The distribution of CNTs along the thickness direction of the polymer matrix can be uniform or functionally graded. Although carbon nanotube reinforced composites or nanocomposites, were used as a single-layer structural element in the early stages of their formation, they

\* Corresponding author at: Azerbaijan University of Architecture and Construction, 1073 Baku, Azerbaijan.

E-mail address: [aavey@ticaret.edu.tr](mailto:aavey@ticaret.edu.tr) (A.H. Sofiyev).

have started to be used as multilayer structural elements in the last few years. Since the effect of thermal environments is critical in the applications of nanocomposite structural elements, the investigation of their stability behavior in thermal environments has always been the focus of attention of researchers. The first attempts to buckling FG-nanocomposite cylindrical shells in thermal environments were made by Shen et al. [10–12]. The solution of the governing equations in these studies was carried out using a singular perturbation technique in conjunction with a two-step perturbation approach. Following these studies various investigations on the buckling and postbuckling behaviors of FG-nanocomposite shells are reported by other research teams using different theories and methods. Among them, Chakraborty et al. [13] studied the stability and vibration analysis of CNT reinforced functional grade laminated composite cylindrical shell panels using a semi-analytical approach. Hieu and Tung [14,15] presented the mechanical and thermomechanical post-buckling behavior of CNT-reinforced composite cylindrical shells surrounded by an elastic medium and subjected to combined mechanical loads in thermal environments. Ghasemi and Soleymani [16] investigated the buckling of functionally graded CNT/fiber/polymer/metal composite panels subjected to hydrostatic pressure, considering the caking and defect issues caused by simultaneous fabrication. Nejati et al. [17] reported thermal buckling of nanocomposite hardened cylindrical shells reinforced with functionally graded wavy carbon nanotubes with temperature-dependent properties. Baccocchi [18] studied the buckling analysis of three-phase CNT/polymer/fiber functionally graded orthotropic plates: The effect of non-uniform distribution of oriented fibers on critical load. Sobhani and Masoodi [19] presented a comprehensive shell approach for vibration of porous nano-enriched polymer composite coupled spheroidal-cylindrical shells. Muc et al. [20] used higher order theories for the buckling and post-buckling studies of shallow spherical shells made of functionally graded materials. Shi et al. [21] studied vibration analysis of combined functionally graded cylindrical-conical shells coupled with annular plates in thermal environment. Avey et al. [22] investigated the thermoelastic stability of CNT patterned conical shells under thermal loading within the framework of shear deformation theory. Sofiyev and Fantuzzi [23] presented the stability analysis of inhomogeneous nanocomposite cylindrical shells within SDT under hydrostatic pressure in the thermal environment. Ipek et al. [24] studied the buckling behavior of nanocomposite plates with functionally graded properties under compression loads in elastic and thermal environments. Kuriakose and Sreehari [25] studied vibration and flutter analysis of damaged composite plates under thermal environment and its passive control using piezoelectric patches.

The number of publications on the bending and stability behavior of multilayer cylindrical shells whose layers are composed of FG-nanocomposites is quite limited. Adopting the concept of FG-nanocomposites, Shen et al. [26] studied the bending analysis of FG-GRC laminated cylindrical panels on elastic foundations in thermal environments by applying a two-step perturbation approach. Monaco et al. [27,28] investigated hygro-thermal static analysis, vibrations and buckling of laminated nanoplates via nonlocal strain gradient theory. Baghbadorani and Kiani [29] studied free vibration analysis of functionally graded cylindrical shells reinforced with graphene platelets. Avey et al. [30,31] solved the free vibration problem of layered functionally graded nanocomposite structures by considering transverse shear stresses and rotational inertia and thermal buckling problem of laminated nanocomposite conical shells by considering transverse shear stresses. Shen et al. [32] examined postbuckling behaviors of pressure-loaded laminated cylindrical shells made of carbon nanotube reinforced composite (FG-CNTRC) with out-of-plane effective Poisson's ratio under thermal environmental conditions using the asymptotic sense by means of a singular perturbation technique in associate with a two-step perturbation approach. Chen et al. [33] reexamined for linear and nonlinear free vibration of porous sandwich cylindrical shells reinforced by graphene platelets by applying a two-step perturbation

approach. Shi et al. [34] presented multilayer heterostructure inhomogeneous model for pressurized functionally graded annular structures with arbitrary elastic property along the radial direction.

The aim of this paper is to perform buckling analysis of multilayer functionally graded carbon nanotube reinforced composite cylindrical shells by extending the first order shear deformation theory proposed for the multilayer homogeneous composite shells to the multilayer functionally graded nanocomposite shells. The modified theory contains only four unknowns, shear correction factors are not used (it is inconvenient to use), and the functions characterizing the distribution of transverse shear stresses in the thickness direction are equal to zero at the upper and lower surfaces, satisfying the assumption of stress-free boundary conditions. It is assumed that carbon nanotubes are evenly distributed over the thickness of each layer and are functionally graded in the form of a pyramid, an inverted pyramid, and a sandglass. The system of governing equations is solved to obtain the critical lateral pressure and mode shapes of multilayer shells composed of FG-NCLs. The accuracy of the presented formulation is achieved by comparing the magnitudes of the LCP with the results available in the literature. In addition, the influences on the critical lateral pressure are reported in detail by considering geometric parameters, CNT distributions, volume fraction of CNTs, change of the order and number of the layers.

The paper is organized as follows: Section 2 provides a basic description and mathematical models of multilayer cylindrical shells made of FG-NCLs, while Section 3 explains the solution procedure. The mechanical properties and design parameters of laminated nanocomposite shells and stability analysis are discussed in Section 4. Finally, Section 5 highlights the main conclusions of this study.

## 2. Methodology

### 2.1. Description of multilayer cylindrical shells made of FG-NCLs

The geometrical configuration of the multilayer cylindrical shell made of FG-NCLs with mean radius  $R$ , total thickness  $h$  and length  $L$ , under the uniform lateral pressure is depicted in Fig. 1. The three orthogonal displacements of an arbitrary point on the multilayer cylindrical shell reference surface in the directions  $x$ ,  $y$  and  $z$  directions are represented as  $u_1, u_2$  and  $u_3$ , respectively. It is postulated that the bonding condition of the layers of the multilayer cylindrical shell, which consists of nanocomposite layers of  $N$  equal thickness ( $\delta = N/h$ ) perfectly bonded to each other, is purely rigid, and that the layers do not break apart during the deformation process. The relationship between the forces and the Airy stress function is assumed to be as follows:  $(N_{11}, N_{22}, N_{12}) = h \left[ \frac{\partial^2 \Phi}{\partial y^2}, \frac{\partial^2 \Phi}{\partial x^2}, -\frac{\partial^2 \Phi}{\partial x \partial y} \right]$ . In the chosen coordinate system, the multilayer cylindrical shell is defined as:

$$\Pi = \{x, y, z : (x, y, z) \in [0, R] \times [0, L] \times [-h/2, +h/2]\} \quad (1)$$

Since bending deformations are negligible except in a region close to the edge supports prior to buckling, the membrane form of the equilibrium equations is commonly used to obtain the pre-buckling forces of cylindrical shells [35–37]. Taking this assumption into account, the anterior buckling features of the multilayer nanocomposite cylindrical shell are denoted by the superscript 0 and take the following form [35]:

$$N_{11}^0 = 0, \quad N_{22}^0 = -PR, \quad N_{12}^0 = 0 \quad (2)$$

where  $N_{pq}^0$  are the membrane forces for the condition with zero initial moments and  $P$  denotes the uniform lateral pressure.

To extend Ambartsumyan's shear deformation theory to functionally graded nanocomposite shells, equivalent material properties need to be estimated to account for the influence of CNTs. For this purpose, multi-scale modeling of CNTs and matrix is performed in the study. Various micromechanical models have been developed to predict the effective material properties of functionally graded nanocomposites, such as the

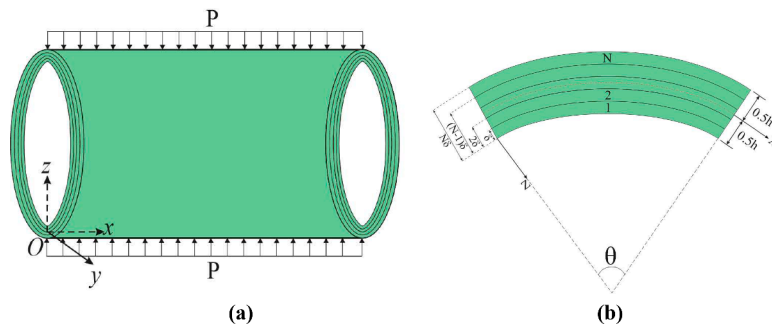


Fig. 1. (a) Multilayer cylindrical shell composed of nanocomposite layers with different CNT-patterns subjected to lateral pressure and (b) the cross section.

Mori-Tanaka model [38,39] and the Voigt model as rule of mixture [40, 41]. The Mori-Tanaka model can be applied to microparticles, and the mixing rule is very useful for determining the effective material properties and responses of functionally graded nanocomposite structural elements. At the nanoscale, both the Mori-Tanaka and Voigt models need to be extended to include small-scale effects. Voigt and Mori-Tanaka models have been shown to have the same effect in predicting the buckling and vibration properties of structural members with various configurations, such as functionally graded ceramic-metal beams, plates and shells [42–44].

The effective material properties are defined based on extended rule of mixture [10–12]. While the effective moduli of elasticity and coefficients of thermal expansion of nanocomposite layers are assumed to be functions of temperature and location, the effective Poisson ratio and density are assumed to be constant since they are weakly dependent on the temperature change and location. Based on these assumptions, the effective mechanical and thermal expansion coefficients of the  $i^{th}$ -layer can be mathematically modeled as follows [10,23,24]:

$$E_{11(\bar{z},T)}^{(i)} = \eta_1^{(i)} V_c^{(i)} E_{11T}^{c(i)} + V_m^{(i)} E_T^{m(i)}, \quad \frac{\eta_2^{(i)}}{E_{22(\bar{z},T)}^{(i)}} = \frac{V_c^{(i)}}{E_{22T}^{c(i)}} + \frac{V_m^{(i)}}{E_T^{m(i)}}, \quad \frac{\eta_3^{(i)}}{G_{12(\bar{z},T)}^{(i)}} = \frac{V_c^{(i)}}{G_{12T}^{c(i)}} + \frac{V_m^{(i)}}{G_T^{m(i)}}, \quad (3)$$

$$G_{13(\bar{z},T)}^{(i)} = G_{12(\bar{z},T)}^{(i)}, \quad G_{23(\bar{z},T)}^{(i)} = 1.2G_{12(\bar{z},T)}^{(i)}, \quad \nu_{12}^{(i)} = V_c^{(i)} \nu_{12}^{c(i)} + V_m^{(i)} \nu^{m(i)}, \quad \rho_t^{(i)} = V_c^{(i)} \rho^{c(i)} + V_m^{(i)} \rho^{m(i)}$$

and

$$\alpha_{11(\bar{z},T)}^{(i)} = \frac{V_c^{(i)} E_{11T}^{c(i)} \alpha_{11T}^{c(i)} + V_m^{(i)} E_T^{m(i)} \alpha_T^{m(i)}}{V_c^{(i)} E_{11T}^{c(i)} + V_m^{(i)} E_T^{m(i)}} \quad (4)$$

$$\alpha_{22(\bar{z},T)}^{(i)} = (1 + \nu_{12}^{c(i)}) V_c^{(i)} \alpha_{22T}^{c(i)} + (1 + \nu^{m(i)}) V_m^{(i)} \alpha_T^{m(i)} - \nu_{12}^{(i)} \alpha_{11(\bar{z},T)}^{(i)}$$

where  $V_c^{(i)}$  and  $V_m^{(i)}$  represent the volume fractions of CNTs and polymer in the  $i^{th}$ -layer, respectively;  $E_{ppT}^{c(i)}$ ,  $G_{pqT}^{c(i)}$  ( $p = 1, 2, q = 1, 2, 3$ ) and  $E_{ppT}^{m(i)}$ ,  $G_{pqT}^{m(i)}$  ( $p = 1, 2, q = 1, 2, 3$ ) denote the modulus of elasticity of the reinforcement and matrix, respectively, in the  $i^{th}$ -layer, while the CNT efficiency parameters  $\eta_q^{(i)}$  ( $q = 1, 2, 3$ ) in the  $i^{th}$ -layer are introduced to capture the effect of load transfer between nanotubes and matrix phase as well as the scale dependent material properties [10]. In addition,  $\alpha_{ppT}^{c(i)}$  and  $\alpha_T^{m(i)}$  denote the thermal expansion coefficients of the CNTs and the polymer in the  $i^{th}$ -layer, respectively.

While many researchers have modeled the mechanical behavior of single-walled carbon nanotube (SWCNT) by taking input from molecular mechanics, several new computational methods such as equivalent continuum models [45], quasi-continuum models [46], and molecular

dynamics simulations [47–51] and developed their applications to nanostructures. In this paper, the CNT efficiency parameter can be determined by comparing the elastic modulus of CNTRCs obtained from MD simulations with those predicted from the mixture rule.

The CNT volume fraction is defined by a gradual change from the inner to the outer surface of the  $i^{th}$ -layer, proposing that,

$$V_c^{(i)} = \Gamma_c V_c^{*(i)} \quad (5)$$

where

$$V_c^{*(i)} = \left( \frac{\rho_c^{(i)}}{m_c^{(i)} \rho_m^{(i)}} - \frac{\rho_c^c}{\rho_m^{(i)}} + 1 \right)^{-1} \quad (6)$$

in which  $m_c^{(i)}$  denotes the mass fraction of CNTs,  $\rho_c^{(i)}$  and  $\rho_m^{(i)}$  are density of CNTs and matrix phase in the layer  $i^{th}$ , respectively. Here  $\Gamma_c$  is the linear function describing the distribution of CNTs along the thickness direction in the  $i^{th}$ -layer, as classified by Shen [12], the profiles in the layers are rhombic prism ( $\diamond$ ), inverted pyramid (V), sandglass (X) and uniform

(U) shaped and modeled as follows (see, Fig. 2) [11]:

$$\frac{V_c^{(i)}}{V_c^{*(i)}} = \begin{cases} U & \text{for } \Gamma_c = 1 \\ V & \text{for } \Gamma_c = 2(0.5 - \bar{z}) \\ \diamond & \text{for } \Gamma_c = 2(1 - 2|\bar{z}|) \\ X & \text{for } \Gamma_c = 4|\bar{z}| \end{cases} \quad (7)$$

## 2.2. Basic relations and equations

The stress components of multilayer cylindrical shells consisting of FG-NCLs with linearly thermoelastic material properties as linear functions of strain and temperature change within SDT can be written as follows [26,30]:

$$\begin{bmatrix} \sigma_{11}^{(i)} \\ \sigma_{22}^{(i)} \\ \sigma_{12}^{(i)} \end{bmatrix} = \begin{bmatrix} K_{11(\bar{z},T)}^{(i)} & K_{12(\bar{z},T)}^{(i)} & 0 \\ K_{21(\bar{z},T)}^{(i)} & K_{22(\bar{z},T)}^{(i)} & 0 \\ 0 & 0 & K_{66(\bar{z},T)}^{(i)} \end{bmatrix} \begin{bmatrix} \epsilon_{11} \\ \epsilon_{22} \\ \gamma_{12} \end{bmatrix} - \begin{bmatrix} \sigma_{11T}^{(i)} \\ \sigma_{22T}^{(i)} \\ 0 \end{bmatrix} \quad (8)$$

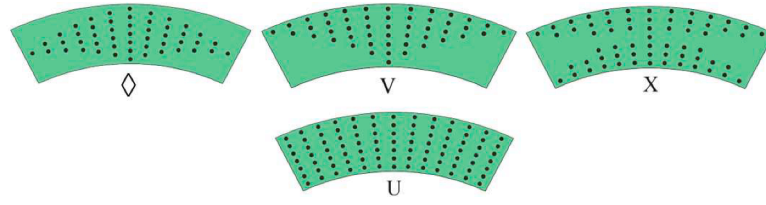


Fig. 2. Shapes of the uniform and linear variations of CNTs in the  $i^{th}$ -layer.

$$\begin{bmatrix} \sigma_{13}^{(i)} \\ \sigma_{23}^{(i)} \end{bmatrix} = \begin{bmatrix} K_{55}^{(i)}(\bar{z}, T) & 0 \\ 0 & K_{44}^{(i)}(\bar{z}, T) \end{bmatrix} \begin{bmatrix} \gamma_{13} \\ \gamma_{23} \end{bmatrix} \quad (9)$$

$$\begin{bmatrix} \epsilon_{11} \\ \epsilon_{12} \\ \gamma_{12} \end{bmatrix} = \begin{bmatrix} e_{11} - z \frac{\partial^2 u_3}{\partial x^2} + \Pi_{1(z,T)}^{(i)} \frac{\partial \Psi_1}{\partial x} \\ e_{22} - z \frac{\partial^2 u_3}{\partial y^2} + \Pi_{2(z,T)}^{(i)} \frac{\partial \Psi_2}{\partial y} \\ \gamma_{012} - 2z \frac{\partial^2 u_3}{\partial x \partial y} + \Pi_{1(z,T)}^{(i)} \frac{\partial \Psi_1}{\partial y} + \Pi_{2(z,T)}^{(i)} \frac{\partial \Psi_2}{\partial x} \end{bmatrix} \quad (14)$$

$$\begin{aligned} \sigma_{11T}^{(i)} &= \begin{bmatrix} K_{11}^{(i)}(\bar{z}, T) & 0 \\ 0 & K_{12}^{(i)}(\bar{z}, T) \end{bmatrix} \begin{bmatrix} \alpha_{11}^{(i)}(\bar{z}, T) \\ \alpha_{22}^{(i)}(\bar{z}, T) \end{bmatrix} \Delta T, \sigma_{22T}^{(i)} \\ &= \begin{bmatrix} K_{21}^{(i)}(\bar{z}, T) & 0 \\ 0 & K_{22}^{(i)}(\bar{z}, T) \end{bmatrix} \begin{bmatrix} \alpha_{11}^{(i)}(\bar{z}, T) \\ \alpha_{22}^{(i)}(\bar{z}, T) \end{bmatrix} \Delta T \end{aligned} \quad (10)$$

where  $e_{11}, e_{22}, \gamma_{012}$  are the linear strain components on the reference surface, defined by

$$e_{11}^0 = \frac{\partial u_1}{\partial x}, \quad e_{22}^0 = \frac{\partial u_2}{\partial y} - \frac{u_3}{R}, \quad e_{12}^0 = \frac{\partial u_2}{\partial x} + \frac{\partial u_1}{\partial y} \quad (15)$$

and  $\Pi_{k(z,T)}^{(i)}$  ( $k = 1, 2$ ) are parameters, defined by

$$\Pi_{1(z,T)}^{(i)} = \int_0^z \frac{1}{K_{55}^{(i)}(\bar{z}, T)} \frac{df^{(i)}}{dz} dz, \quad \Pi_{2(z,T)}^{(i)} = \int_0^z \frac{1}{K_{44}^{(i)}(\bar{z}, T)} \frac{df^{(i)}}{dz} dz \quad (16)$$

where  $\sigma_{pq}^{(i)}$  and  $\sigma_{ppT}^{(i)}$  ( $p = 1, 2, q = 1, 2, 3$ ) indicate the stresses and thermal stresses in the  $i^{th}$ -layer,  $\epsilon_{pq}$  indicate the strains,  $\Delta T = T - T_0$  is the temperature change in which  $T_0$  is the reference temperature, at  $T_0$  the thermal strains are absent and the elements of elastic constant tensor  $K_{pq}^{(i)}$  are formed from effective material properties:

The stress resultants are obtained using the components of stress field as under the SDT assumptions s [35–37]:

$$K_{11}^{(i)}(\bar{z}, T) = \frac{E_{11}^{(i)}(\bar{z}, T)}{1 - \nu_{12}^{(i)} \nu_{21}^{(i)}}, \quad K_{22}^{(i)}(\bar{z}, T) = \frac{E_{22}^{(i)}(\bar{z}, T)}{1 - \nu_{12}^{(i)} \nu_{21}^{(i)}}, \quad K_{12}^{(i)}(\bar{z}, T) = \nu_{21}^{(i)} K_{11}^{(i)}(\bar{z}, T) = \nu_{12}^{(i)} K_{22}^{(i)}(\bar{z}, T) = K_{21}^{(i)}(\bar{z}, T), \quad (11)$$

$$K_{44}^{(i)}(\bar{z}, T) = G_{23}^{(i)}(\bar{z}, T), \quad K_{55}^{(i)}(\bar{z}, T) = G_{13}^{(i)}(\bar{z}, T), \quad K_{66}^{(i)}(\bar{z}, T) = G_{12}^{(i)}(\bar{z}, T).$$

in which  $-\frac{1}{2} + \frac{i-1}{N} \leq \bar{z} \leq -\frac{1}{2} + \frac{i}{N}$ .

The shear stresses  $\sigma_q^{(i)}$  ( $q = 1, 2$ ) in the  $i^{th}$ -layer are expressed as [30, 31,36]:

$$[N_{pq}, Q_p, M_{pq}] = \sum_{i=1}^N \int_{z_{i-1}}^{z_i} [\sigma_{pq}^{(i)}, \sigma_{p3}^{(i)}, z\sigma_{pq}^{(i)}] dz \quad (17)$$

$$\sigma_{33}^{(i)} = 0, \quad \sigma_{p3}^{(i)} = \frac{f^{(i)}(z)}{dz} \Psi_p(x, y), \quad (p = 1, 2) \quad (12)$$

The thermal stress resultants ( $N_{pp}^T, M_{pp}^T$ ) caused by high temperature are found as follows [11,22]:

where then symbols  $\Psi_p(x,y)$  represent the rotation of the normal to mid-plane about  $y$  and  $x$  axes,  $f^{(i)}(z)$  represent shape functions in the  $i^{th}$ -layer determining the distribution of the transverse shear strains and stresses along the thickness and are used as follows [36,37]:

$$(N_{11}^T, M_{11}^T) = \sum_{i=1}^N \int_{z_{i-1}}^{z_i} \begin{bmatrix} K_{11}^{(i)}(\bar{z}, T) & 0 \\ 0 & K_{12}^{(i)}(\bar{z}, T) \end{bmatrix} \begin{bmatrix} \alpha_{11}^{(i)}(\bar{z}, T) \\ \alpha_{22}^{(i)}(\bar{z}, T) \end{bmatrix} (1, z) \Delta T dz, \quad (18)$$

$$\frac{df^{(i)}(z)}{dz} = 1 - 4z^2 \quad (13)$$

$$(N_{22}^T, M_{22}^T) = \sum_{i=1}^N \int_{z_{i-1}}^{z_i} \begin{bmatrix} K_{21}^{(i)}(\bar{z}, T) & 0 \\ 0 & K_{22}^{(i)}(\bar{z}, T) \end{bmatrix} \begin{bmatrix} \alpha_{11}^{(i)}(\bar{z}, T) \\ \alpha_{22}^{(i)}(\bar{z}, T) \end{bmatrix} (1, z) \Delta T dz.$$

By combining Eqs. (5), (8), (9) and (11), the strain components for multilayer cylindrical shells as functions of the strain components and the curvature change at the reference surface in the SDT framework can be written as follows:

Using Eqs. (8), (9), (14), (17) and (18) together, the governing equations for multilayer cylindrical shells composed of FG-NCLs subjected to the lateral pressure can be expressed as:

$$\begin{bmatrix} L_{11} & L_{12} & L_{13} & L_{14} \\ L_{21} & L_{22} & L_{23} & L_{24} \\ L_{31} & L_{32} & L_{33} & L_{34} \\ L_{41} & L_{42} & L_{43} & L_{44} \end{bmatrix} \begin{bmatrix} \Phi \\ u_3 \\ \Psi_1 \\ \Psi_2 \end{bmatrix} = \begin{bmatrix} 0 \\ 0 \\ 0 \\ 0 \end{bmatrix} \quad (19)$$

where  $L_{pq}$  are differential operators, are described in Appendix A.

### 3. Solution procedure

For the two end edges of the multilayer cylindrical shell composed of FG-NCLs, the boundary condition is assumed to be simply supported and expressed as [11,36,37]:

$$\text{At } x = 0, L \quad u_3 = \frac{\partial^2 \Phi}{\partial y^2} = \Psi_2 = M_{11} = 0 \quad (20)$$

where the closed or periodicity condition is expressed as

$$\int_0^{2\pi R} \frac{\partial u_2}{\partial y} dy = 0 \quad (21)$$

The solution of (19) are sought as follows [35,37]:

$$\Phi = C_1 \sin\left(\frac{m\pi}{L}x\right) \sin\left(\frac{n}{R}y\right), \quad u_3 = C_2 \sin\left(\frac{m\pi}{L}x\right) \sin\left(\frac{n}{R}y\right), \quad (22)$$

$$\Psi_1 = C_3 \cos\left(\frac{m\pi}{L}x\right) \sin\left(\frac{n}{R}y\right), \quad \Psi_2 = C_4 \sin\left(\frac{m\pi}{L}x\right) \cos\left(\frac{n}{R}y\right)$$

where  $C_q$  are unknown amplitudes,  $m$  and  $n$  are integer values.

By introducing (22) into Eq. (19), and considering (2), by performing the Galerkin procedure, after some mathematical manipulations, yields:

$$\begin{bmatrix} F_{11} & -F_{12} & F_{13} & F_{14} \\ F_{21} & -F_{22} & F_{23} & F_{24} \\ F_{31} & -F_{32} & F_{33} & F_{34} \\ F_{41} & PRF_{42} & F_{43} & F_{44} \end{bmatrix} \begin{bmatrix} C_1 \\ C_2 \\ C_3 \\ C_4 \end{bmatrix} = \begin{bmatrix} 0 \\ 0 \\ 0 \\ 0 \end{bmatrix} \quad (23)$$

$$\begin{aligned} E_{117}^{c(i)} &= 6.18387 - 2.86 \times 10^{-3}T + 4.22867 \times 10^{-6}T^2 - 2.2724 \times 10^{-9}T^3 \\ E_{227}^{c(i)} &= 7.75348 - 3.58 \times 10^{-3}T + 5.30057 \times 10^{-6}T^2 - 2.84868 \times 10^{-9}T^3 \\ G_{12}^{c(i)} &= 1.80126 + 0.77845 \times 10^{-3}T - 1.1279 \times 10^{-6}T^2 + 4.93484 \times 10^{-10}T^3 \\ \alpha_{117}^{c(i)} &= (-1.12148 + 2.289 \times 10^{-2}T - 2.88155 \times 10^{-5}T^2 + 1.13253 \times 10^{-8}T^3) \cdot 10^{-6}/K \\ \alpha_{227}^{c(i)} &= (5.43874 - 9.95498 \times 10^{-4}T + 3.13525 \times 10^{-7}T^2 - 3.56332 \times 10^{-12}T^3) \cdot 10^{-6}/K \end{aligned} \quad (27)$$

where  $F_{pq}$  are described in Appendix B.

When the determinant of the  $4 \times 4$  type matrix in Eq. (23) is expanded according to the fourth row and first column and set to zero, the following equation is obtained for the analytical expression determining the nondimensional critical lateral pressure (ND-LCP) of the laminated shells formed from the FG-NCLs in the thermal environment:

$$P_{1sd}^{lcr} = \frac{b^2}{E_{T_0}^{m(i)} n^2 \pi^2 R} \frac{F_{41}U_1 + F_{43}U_3 + F_{44}U_4}{U_2} \quad (24)$$

where  $E_{T_0}^{m(i)}$  is the modulus of elasticity in the  $i^{th}$ -layer at  $T_0 = 300(K)$  (at room temperature) and  $U_q (q = 1, 2, \dots, 4)$  are defined by

**Table 1**

The elastic properties and thermal expansion coefficients for (10, 10) SWCNT in the  $i^{th}$ -layer under temperature environments.

(in K)	(in TPa)			(in 1/K)	
Temperature	$E_{117}^{c(i)}$	$E_{227}^{c(i)}$	$G_{127}^{c(i)}$	$\alpha_{117}^{c(i)}/10^6$	$\alpha_{227}^{c(i)}/10^6$
300	5.6451	7.0796	2.0665	3.4579	5.1682
450	5.5461	6.9563	2.3728	4.3758	5.0539
600	5.4994	6.8984	2.9283	4.6852	4.9535
750	5.4588	6.8482	3.8325	4.6152	4.8670

$$U_1 = - \begin{vmatrix} F_{12} & F_{13} & F_{14} \\ F_{22} & F_{23} & F_{24} \\ F_{32} & F_{33} & F_{34} \end{vmatrix}, \quad U_2 = \begin{vmatrix} F_{11} & F_{13} & F_{14} \\ F_{21} & F_{23} & F_{24} \\ F_{31} & F_{33} & F_{34} \end{vmatrix}, \quad U_3 = - \begin{vmatrix} F_{11} & F_{12} & F_{14} \\ F_{21} & F_{22} & F_{24} \\ F_{31} & F_{32} & F_{34} \end{vmatrix}, \quad U_4 = \begin{vmatrix} F_{11} & F_{12} & F_{13} \\ F_{21} & F_{22} & F_{23} \\ F_{31} & F_{32} & F_{33} \end{vmatrix} \quad (25)$$

The minimum value of the ND-LCP is found by minimizing (24) according to the longitudinal and circumferential wave numbers. When transverse shear strains are not taken into account, the magnitudes of ND-LCP are found in the framework of KLT.

### 4. Numerical results

#### 4.1. Material properties in thermal environments

The numerical investigations for the stability of multilayer cylindrical shells composed of FG-NCLs subjected to the uniform lateral pressure in thermal environments are discussed in this section. To examine the accuracy and effectiveness of the present solutions, two comparison examples are first carried out. The effective material properties of poly methyl methacrylate (PMMA) and (10, 10) SWCNT with length = 9.26nm, radius = 0.68nm, tubethickness = 0.067nm,  $\nu_{12}^{c(i)} = 0.175$  that make up the nanocomposite in the layers are defined as, respectively [10–12]:

$$\begin{aligned} E_T^{m(i)} &= (3.52 - 0.0034T) \times 10^9 \text{ (Pa)}, \quad \nu^{m(i)} = 0.34, \quad \alpha_T^{m(i)} \\ &= 45(1 + 0.0005\Delta T) \times 10^{-6}/K \end{aligned} \quad (26)$$

and

At reference temperature, that is, at  $T_0 = 300K$ ,  $\alpha_{T_0}^{m(i)} = 45 \times 10^{-6}/K$ ,  $E_{T_0}^{m(i)} = 2.5 \times 10^9 Pa$ .

The magnitudes of elastic properties and thermal expansion coefficients of the (10, 10) SWCNT in the  $i^{th}$ -layer for different  $Tare$

**Table 2**

Magnitudes of CNT efficiency parameters in the  $i^{th}$ -layer.

$\nu_*^{c(i)}$	$\eta_1^{(i)}$	$\eta_2^{(i)}$	$\eta_3^{(i)}$
0.12	0.137	1.626	0.715
0.17	0.142	1.626	1.138
0.23	0.141	1.585	1.109

**Table 3**  
Comparison the magnitudes of LCP for single-layer cylindrical shells patterned by CNTs based on the SDT with the results of Shen [11].

Patterns type T (K)	$P_{sdt}^{Lcr}$ (inkPa), ( $n_{cr}$ ),			
	Uniform $V_s^{(1)} = 0.12$		Sandglass profile	
	Ref. [11]	Present study	Ref. [11]	Present study
300	474.80(5)	473.74(5)	558.72(6)	557.36(6)
500	367.35 (6)	367.29 (6)	432.75(6)	431.33(6)
	$V_s^{(1)} = 0.28$			
300	943.62(6)	942.46(6)	1234.8(6)	1235.20(6)
500	723.33 (6)	723.68(6)	963.81(6)	958.93(6)

calculated using the Eq. (27) and listed in Table 1.

The corresponding values of CNT efficiency parameters  $\eta_q^{(i)}$  ( $q = 1, 2, 3$ ) in the  $i^{th}$ -layer are tabulated in Table 2. As it is known, the charge transfer between nanotube and polymeric phases is less than perfect due to surface effects, strain gradient effects, intermolecular coupled stress effects, etc. To consider these effects, the CNT efficiency parameters  $\eta_q^{(i)}$  are included in the Eq. (3). The magnitudes of  $\eta_q^{(i)}$  are determined by matching the elastic modulus of nanocomposites estimated by Han and Elliott [9] with molecular dynamics simulations with the values estimated by the extended mixing rule in the Eq. (3).

4.2. Comparative examples

The critical lateral pressure of FG-nanocomposite and orthotropic cylindrical shells are calculated and compared with the results in the open literature. The comparison results are listed in Tables 3 and 4. Here the magnitude of the LCP is found using  $P_{sdt}^{Lcr} = P_{1sdt}^{Lcr} E_{T_0}^{m(i)}$  in Eq. (24).

Example 1: The magnitudes of LCP for single-layer nanocomposite cylindrical shells patterned by CNTs with the uniform and sandglass-model based on the SDT under two thermal environmental conditions are compared with the results of Shen [11] and are presented in Table 3 for ( $i = 1$ ). The material properties are taken from the study of Ref. [11] and can be carried out from (26) and (27) in thermal environments. The following geometrical data are used:  $L^2 = 100Rh$ ,  $h = 0.002m$ ,  $R = 30h$  [11]. Since the number of longitudinal waves corresponding to the LCP is equal to one, it is not included in Table 3, and the values of the number of circumferential waves are shown in the table. The magnitudes of the LCP for uniform and sandglass shaped nanocomposite cylinders based

**Table 4**  
Comparison the LCP for homogeneous orthotropic cylindrical shells within SDTs.

	L/R = 1		L/R = 2		L/R = 5	
	Ref. [52]	Present SDT	Ref. [52]	Present SDT	Ref. [52]	Present SDT
	$P_{sdt}^{Lcr}$ (kPa), ( $n_{cr}$ )					
M1	3560(7)	3561(7)	1498(5)	1496(5)	628(4)	628(4)
M2	11,192(4)	11,192(4)	5962 (3)	5961(3)	2522(2)	2522(2)

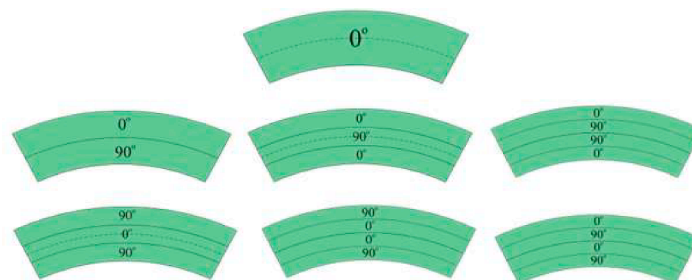


Fig. 3. The cross sections of multilayer nanocomposite orthotropic cylindrical shells.

on the SDT for the same circumferential wave numbers in good agreement with the results of Shen [11] at two thermal environmental conditions.

Example 2: The LCP of single-layer homogenous orthotropic cylindrical shells (in kPa) are calculated with various L/R ratio and listed in Table 4. These values are compared with the appropriate magnitudes obtained from the Li and Lin [52]. In computations are used special case of the expression (24). Two kinds of orthotropic materials are used. (Material 1):  $E_{11}^{(1)} = 149.66 \text{ GPa}$ ,  $E_{22}^{(1)} = 9.93 \text{ GPa}$ , (Material 2):  $E_{11}^{(1)} = 9.93 \text{ GPa}$ ,  $E_{22}^{(1)} = 149.66 \text{ GPa}$ , and shear moduli and Poisson's ratio of both materials (M1 and M2) are  $G_{12}^{(1)} = G_{13}^{(1)} = G_{23}^{(1)} = 4.48 \text{ GPa}$ ,  $\nu_{12}^{(1)} = 0.28$  [52]. The cylindrical shell characteristics are as follows:  $R/h = 30$ ,  $L/R = 1, 2$  and  $5$ . The number of circumferential waves ( $n_{cr}$ ) corresponding to the LCP is presented in brackets. It is clearly seen that the present results are in good agreement with those in the literature and show that the derived basic equations and the obtained formula for this study are correct.

4.3. Parametric studies

In what follows, we analyze the sensitivity of the ND-LCP (or  $P_1^{Lcr}$ ) to FG-nanocomposites, CNT patterns, SDT formulation, change of temperature, by considering the ratios  $100\% \times \left( \frac{P_{1FG}^{Lcr} - P_{1U}^{Lcr}}{P_{1U}^{Lcr}}, \frac{P_{1KT}^{Lcr} - P_{1sdt}^{Lcr}}{P_{1KT}^{Lcr}}, \frac{P_{1T}^{Lcr} - P_{1T_0}^{Lcr}}{P_{1T_0}^{Lcr}} \right)$ . Four of the main parameters affecting the ND-LCP are the transverse shear strains, the temperature rise, the CNT-patterns and arrangement of layers. Since the number of longitudinal waves is equal to one, it is not included in the tables. The cross-sections of cylindrical shells with six symmetric and anti-symmetric layers used in numerical calculations and the (0°)-single-layer for comparison are presented in Fig. 3. In the analysis presented below, the magnitudes of the ND-CLP for single-layer and multilayer cylindrical shells composed of FG-NCLs in the thermal environments are calculated in the framework of KLT and SDT.

The variation of ND-LCP ND- LCP and circumferential wave numbers of single- and multilayer cylindrical shells consisting of symmetric and anti-symmetric FG-NCLs of uniform, inverted pyramid, rhombic prism and sandglass patterns according to the increase of the L/Rin thermal environments are listed in Tables 5 and 6. The cylindrical shell dimensions are:  $h = 0.002m$ ,  $R/h = 20$ , the volume fraction  $V_s^{c(i)}$  is 0.28, other material properties are found by the Eqs. (26) and (27) depending on the temperature rise. The ND-LCP values and corresponding

**Table 5**

Variation of the ND-LCP and circumferential wave numbers of single- and multilayer cylindrical shells consisting of uniform and FG-NCLs against the  $L/R$  with  $T = 300$  and  $500(K)$ .

$L/R$	Number and arrangement of layers	$P_{1st}^{Lcr} \times 100, (n_{cr}), T = 300 (K)$							
		$U$		$V$		$\diamond$		$X$	
		SDT	KLT	SDT	KLT	SDT	KLT	SDT	KLT
0.25	(0°)	1.550 (24)	5.77 (25)	1.594 (24)	4.565 (28)	1.515 (23)	3.601 (28)	1.628 (24)	7.120 (33)
	(0°/90°)	2.627 (15)	5.344 (13)	2.306 (15)	4.432 (16)	2.240 (16)	3.761 (13)	2.473 (16)	4.780 (13)
	(0°/90°/0°)	1.998 (27)	7.760 (25)	2.000 (21)	5.988 (20)	2.360 (21)	6.060 (21)	1.793 (25)	8.712 (29)
	(90°/0°/90°)	2.969 (24)	8.104 (7)	2.910 (17)	6.192 (8)	3.100 (16)	6.120 (8)	2.715 (30)	9.252 (6)
	(0°/90°/0°/90°)	2.876 (35)	13.22 (13)	2.548 (33)	9.032 (16)	3.122 (23)	8.396 (13)	2.548 (39)	12.92 (13)
	(0°/90°/90°/0°)	2.428 (28)	11.23 (20)	2.418 (22)	7.612 (16)	2.938 (20)	7.896 (15)	2.083 (26)	13.01 (23)
	(90°/0°/0°/90°)	3.012 (40)	11.330 (8)	2.978 (20)	7.712 (10)	3.186 (20)	7.952 (11)	2.747 (40)	13.21 (7)
0.50	(0°)	0.738 (14)	1.309 (16)	0.728 (13)	1.148 (14)	0.639 (13)	0.903 (14)	0.833 (13)	1.784 (17)
	(0°/90°)	1.148 (6)	1.403 (7)	0.898 (8)	1.133 (8)	0.832 (7)	1.002 (7)	1.027 (7)	1.262 (7)
	(0°/90°/0°)	1.050 (12)	1.949 (13)	0.988 (12)	1.502 (11)	1.036 (10)	1.514 (10)	1.013 (11)	2.182 (15)
	(90°/0°/90°)	1.828 (5)	2.581 (4)	1.527 (5)	1.976 (5)	1.479 (5)	1.823 (5)	2.015 (5)	3.642 (3)
	(0°/90°/0°/90°)	1.928 (8)	3.692 (8)	1.511 (10)	2.305 (8)	1.583 (8)	2.184 (7)	1.859 (9)	3.317 (6)
	(0°/90°/90°/0°)	1.498 (9)	2.819 (10)	1.308 (10)	1.955 (8)	1.428 (8)	2.014 (8)	1.348 (13)	3.266 (12)
	(90°/0°/0°/90°)	2.068 (6)	3.235 (4)	1.599 (7)	2.169 (5)	1.644 (6)	2.126 (6)	2.231 (6)	3.856 (4)
0.75	(0°)	0.425 (10)	0.586 (11)	0.407 (9)	0.518 (10)	0.342 (9)	0.408 (9)	0.505 (10)	0.794 (11)
	(0°/90°)	0.628 (5)	0.704 (5)	0.500 (6)	0.542 (6)	0.480 (5)	0.521 (5)	0.569 (5)	0.642 (5)
	(0°/90°/0°)	0.637 (8)	0.877 (8)	0.569 (8)	0.692 (7)	0.573 (6)	0.694 (7)	0.588 (8)	0.974 (10)
	(90°/0°/90°)	1.302 (4)	1.680 (3)	1.001 (4)	1.200 (4)	0.942 (4)	1.078 (4)	1.517 (4)	2.116 (3)
	(0°/90°/0°/90°)	1.231 (5)	1.629 (5)	0.840 (6)	1.092 (6)	0.864 (5)	1.066 (5)	1.240 (5)	1.600 (5)
	(0°/90°/90°/0°)	0.935 (7)	1.278 (7)	0.752 (6)	0.922 (6)	0.837 (7)	0.958 (5)	0.877 (9)	1.460 (8)
	(90°/0°/0°/90°)	1.393 (4)	1.841 (4)	1.010 (5)	1.176 (4)	0.972 (5)	1.106 (4)	1.621 (4)	2.293 (3)
1.0	(0°)	0.274 (8)	0.333 (8)	0.261 (7)	0.301 (7)	0.214 (7)	0.237 (7)	0.338 (8)	0.452 (8)
	(0°/90°)	0.452 (5)	0.477 (4)	0.315 (5)	0.347 (5)	0.340 (5)	0.372 (4)	0.420 (5)	0.443 (4)
	(0°/90°/0°)	0.403 (7)	0.5007 (7)	0.354 (6)	0.410 (6)	0.379 (5)	0.422 (5)	0.404 (7)	0.558 (7)
	(90°/0°/90°)	1.072 (3)	1.254 (3)	0.854 (3)	0.937 (3)	0.744 (4)	0.853 (3)	1.266 (3)	1.691 (3)
	(0°/90°/0°/90°)	0.848 (4)	1.024 (4)	0.594 (5)	0.685 (5)	0.644 (4)	0.694 (4)	0.845 (4)	1.009 (4)
	(0°/90°/90°/0°)	0.608 (4)	0.746 (5)	0.508 (5)	0.577 (5)	0.542 (4)	0.609 (4)	0.600 (6)	0.837 (6)
	(90°/0°/0°/90°)	1.106 (3)	1.269 (3)	0.722 (4)	0.857 (4)	0.694 (4)	0.779 (4)	1.336 (3)	1.710 (3)

circumferential wave numbers of the multilayer FG-nanocomposite cylindrical shells for all patterns, layer arrangement and number reduce with the rise of the  $L/R$  at the fixed value of the temperature.

In the framework of SDT, the influences of FG-patterns on the  $P_{1st}^{Lcr}$  compared to the uniform patterns generally show an irregularity with increasing  $L/R$  and temperature rise. For instance, the most pronounced pattern effects on the  $P_{1st}^{Lcr}$  occur in the (90°/0°/0°/90°)-array cylindrical shells consisting of  $\diamond$ -originating layers are (-37.25%), (-36.21%) and (-37.07%), at  $T = 300 (K)$ ,  $500 (K)$  and  $700 (K)$ , respectively, when  $L/R = 1.0$  (see, Tables 5 and 6).

Although the influences of transverse shear strains on the ND-LCP differ with the change of  $L/R$  and temperature rise, the most prominent effect always occurs in cylindrical shells consisting of sandglass-originating layers. For example, At  $T = 300 (K)$ , the most prominent effects of transverse shear strains on the ND-LCP of multilayer shells occur in (0°/90°/90°/0°)-array shell composed of layers originating from sandglass model with 84% and 28.32%, as the  $L/R$  varies between 0.25 and 1.0, respectively. The closest to those influences is in the (0°/90°/90°/0°)-array shells consisting of U-originating layers, it is lower approximately 5.61%, and 8.81%, respectively, as the  $L/R$  varies between 0.25 and 1.0 (see, Table 5). For  $T = 500 (K)$ , the most significant transverse shear strains effects on the ND-LCP occur in (0°/90°/90°/0°)-array shells originating from sandglass with 84.02% and 27.18%, respectively, when the  $L/R$  varies between 0.25 and 1.0. It should be emphasized that when  $L/R=0.75$ , the greatest transverse shear strains effect occurs in the (0°/90°/0°)-sandwich shell with the 39.54%. The closest case to those effects occurs in the (0°/90°/90°/0°)-array shells consisting of U- originating layers and is approximately 6.5% and 3.03% lower as  $L/R = 0.25$  and  $1.0$  (see, Table 5). At  $T = 700 (K)$ , the most prominent effects of transverse shear strains on the ND-LCP of multilayer shells occur in (0°/90°/90°/0°)-array shells composed of layers originating from sandglass-model with 83.42% and 26.47%, respectively, when the  $L/R$  varies between 0.25 and 1.0 (see, Table 6). The effect of transverse shear strains on ND-LCP significantly reduces for all

pattern types, in the arrangement and number of layers, as the  $L/R$  increment (see, Table 6).

When the  $L/R$  ratio is changed for all values of  $T$ , as the  $P_{1st}^{Lcr}$  of multilayer cylindrical shells is compared with the  $P_{1st}^{Lcr}$  of (0°) single-layer shell, it is revealed that the most significant differences occur in (90°/0°/90°) and (90°/0°/0°/90°)-arrangement shells. It is seen that the least difference occurs for ND-LCP in (0°/90°/0°)-arrangement shell. In addition, with the rise of  $T$ , the effect of layer arrangement on ND-LCP reduces (see, Tables 5 and 6). In the SDT framework, the effects of temperature rise on the  $P_{1st}^{Lcr}$  generally increase irregularly as  $L/R$  increases. The most prominent effect on the ND-LCP is (-8.55%) in the (0°/90°/90°/0°)-alignment shells with uniform patterns when comparing ND-LCPs at  $T = 500 (K)$  and  $T = 300 (K)$ , while that effect is (+10.4%) in X-originating (90°/0°/0°/90°)-arrangement shells when comparing ND-LCPs for  $T = 700 (K)$  and  $T = 300 (K)$  (see, Tables 5 and 6).

The distribution of the magnitudes of the ND- LCP and circumferential wave numbers of single-layer and multilayer cylindrical shells consisting of symmetric and anti-symmetric FG-NCLs with uniform, inverted pyramid, rhombic prism and sandglass patterns according to the rise of  $R/h$  in thermal environments within SDT and KLT are listed in Table 7 and Figs. 4–9. In the formation of Table 7, all values except  $L/R$  are the data used for the formation of the previous tables. The magnitudes of ND-LCP and corresponding circumferential wave numbers of the multilayer FG-nanocomposite cylindrical shells for all patterns, layer arrangement and number reduce with the rise of the  $R/h$  at the fixed value of the temperature. For  $T = 300 (K)$  and when the  $R/h$  ratio increases from 25 to 50, the most pronounced pattern effects on the ND-LCP occur in multilayer shell with different arrays and number of layers, consisting of  $\diamond$ - and V- originating layers. For example, the most prominent pattern effect (-38.28%) occurs in the (90°/0°/0°/90°)-array cylindrical shells with  $\diamond$ -originating layers for  $R/h = 50$ . For  $T = 500 (K)$ , the most prominent pattern effects on the ND-LCP occur in shells consisting of inverted pyramid and  $\diamond$ -originating layers, whereas

**Table 6**

Variation of the ND-LCP and circumferential wave numbers of single- and multilayer cylindrical shells consisting of uniform and FG-NCLs according to  $L/R$  with  $T = 700$  (K).

$L/R$	Number and arrangement of layers	$P_1^{Lcr} \times 100, (n_{cr}), T = 500$ (K)								
		$U$		$V$		$\diamond$		$X$		
		SDT	KLT	SDT	KLT	SDT	KLT	SDT	KLT	
0.25	(0°)	1.549 (24)	5.183 (32)	1.593 (23)	4.525 (28)	1.513 (23)	3.571 (28)	1.627 (24)	7.054 (33)	
	(0°/90°)	2.594 (17)	5.272 (13)	2.153 (18)	4.404 (17)	2.232 (14)	3.711 (13)	2.467 (17)	4.724 (13)	
	(0°/90°/0°)	2.013 (26)	7.644 (25)	2.080 (18)	5.852 (21)	2.362 (20)	5.920 (20)	1.779 (24)	8.600 (29)	
	(90°/0°/90°)	2.955 (30)	7.984 (7)	2.900 (16)	6.100 (8)	3.101 (20)	6.024 (8)	2.715 (29)	9.128 (6)	
	(0°/90°/0°/90°)	2.871 (38)	12.970 (13)	2.541 (34)	8.880 (16)	3.122 (21)	8.248 (13)	2.551 (38)	12.680 (13)	
	(0°/90°/90°/0°)	2.482 (20)	11.040 (20)	2.412 (28)	7.496 (16)	2.895 (23)	7.760 (15)	2.044 (30)	12.790 (23)	
	(90°/0°/0°/90°)	3.012 (40)	11.140 (8)	2.966 (22)	7.596 (10)	3.182 (23)	7.808 (11)	2.745 (40)	12.990 (7)	
	0.5	(0°)	0.736 (14)	1.297 (16)	0.726 (13)	1.138 (14)	0.636 (13)	0.896 (14)	0.831 (13)	1.767 (16)
		(0°/90°)	1.154 (8)	1.386 (7)	0.898 (8)	1.120 (8)	0.854 (8)	0.989 (7)	1.031 (7)	1.248 (7)
(0°/90°/0°)		1.083 (13)	1.921 (13)	0.961 (10)	1.481 (11)	1.045 (9)	1.490 (10)	0.970 (13)	2.154 (15)	
(90°/0°/90°)		1.835 (5)	2.545 (4)	1.496 (5)	1.946 (5)	1.479 (5)	1.795 (5)	2.002 (5)	3.245 (4)	
(0°/90°/0°/90°)		1.903 (8)	3.328 (6)	1.420 (8)	2.267 (8)	1.578 (8)	2.148 (7)	1.831 (8)	3.260 (6)	
(0°/90°/90°/0°)		1.452 (10)	2.770 (10)	1.281 (9)	1.926 (8)	1.400 (9)	1.979 (8)	1.339 (12)	3.210 (12)	
(90°/0°/0°/90°)		2.059 (6)	3.185 (4)	1.561 (6)	2.140 (5)	1.600 (6)	2.089 (6)	2.222 (6)	3.797 (4)	
0.75		(0°)	0.428 (9)	0.581 (11)	0.405 (9)	0.514 (10)	0.340 (9)	0.405 (9)	0.504 (10)	0.787 (11)
		(0°/90°)	0.643 (5)	0.696 (5)	0.478 (6)	0.536 (6)	0.478 (5)	0.515 (5)	0.564 (5)	0.635 (5)
	(0°/90°/0°)	0.637 (8)	0.864 (8)	0.544 (8)	0.683 (7)	0.544 (7)	0.683 (7)	0.581 (9)	0.961 (10)	
	(90°/0°/90°)	1.292 (4)	1.662 (3)	1.000 (4)	1.182 (4)	0.922 (4)	1.062 (4)	1.508 (4)	2.087 (3)	
	(0°/90°/0°/90°)	1.168 (5)	1.602 (5)	0.862 (6)	1.075 (6)	0.921 (5)	1.050 (5)	1.173 (5)	1.572 (5)	
	(0°/90°/90°/0°)	0.870 (7)	1.256 (7)	0.739 (6)	0.908 (6)	0.786 (5)	0.943 (5)	0.877 (9)	1.436 (8)	
	(90°/0°/0°/90°)	1.352 (4)	1.810 (4)	0.985 (4)	1.161 (4)	0.972 (5)	1.090 (4)	1.601 (4)	2.263 (3)	
	1.0	(0°)	0.273 (8)	0.330 (8)	0.259 (7)	0.299 (7)	0.213 (7)	0.235 (7)	0.336 (8)	0.448 (8)
		(0°/90°)	0.428 (4)	0.472 (4)	0.312 (5)	0.343 (5)	0.348 (5)	0.368 (4)	0.420 (5)	0.439 (4)
(0°/90°/0°)		0.403 (7)	0.500 (6)	0.336 (6)	0.405 (6)	0.369 (6)	0.416 (5)	0.404 (7)	0.551 (7)	
(90°/0°/90°)		1.048 (3)	1.237 (3)	0.798 (4)	0.927 (3)	0.734 (4)	0.843 (3)	1.259 (3)	1.665 (3)	
(0°/90°/0°/90°)		0.828 (4)	1.007 (4)	0.560 (5)	0.674 (5)	0.603 (4)	0.684 (4)	0.801 (4)	0.993 (4)	
(0°/90°/90°/0°)		0.556 (5)	0.733 (5)	0.487 (5)	0.568 (5)	0.542 (4)	0.600 (4)	0.600 (6)	0.824 (6)	
(90°/0°/0°/90°)		1.088 (3)	1.252 (3)	0.732 (4)	0.845 (4)	0.694 (4)	0.767 (4)	1.282 (3)	1.685 (3)	
$T = 700$ (K)										
0.25		(0°)	1.549 (24)	5.161 (32)	1.592 (23)	4.506 (28)	1.512 (23)	3.557 (28)	1.627 (24)	7.022 (33)
	(0°/90°)	2.596 (18)	5.252 (12)	2.153 (18)	4.460 (18)	2.215 (16)	3.681 (13)	2.460 (14)	4.704 (13)	
	(0°/90°/0°)	2.024 (25)	7.588 (25)	1.998 (21)	5.812 (21)	2.353 (19)	5.876 (20)	1.779 (24)	8.540 (29)	
	(90°/0°/90°)	2.951 (30)	7.920 (7)	2.900 (16)	6.064 (8)	3.073 (14)	5.980 (8)	2.713 (30)	9.064 (6)	
	(0°/90°/0°/90°)	2.862 (39)	12.850 (13)	2.537 (26)	8.804 (16)	3.100 (22)	8.188 (12)	2.543 (40)	12.560 (13)	
	(0°/90°/90°/0°)	2.428 (28)	10.940 (20)	2.405 (23)	7.436 (16)	2.907 (20)	7.688 (15)	2.102 (28)	12.680 (23)	
	(90°/0°/0°/90°)	3.011 (40)	11.040 (8)	2.967 (23)	7.540 (10)	3.182 (21)	7.740 (11)	2.746 (40)	12.880 (7)	
	0.5	(0°)	0.735 (14)	1.292 (16)	0.725 (13)	1.133 (14)	0.635 (13)	0.892 (14)	0.831 (13)	1.759 (16)
		(0°/90°)	1.091 (7)	1.377 (7)	0.884 (9)	1.168 (7)	0.872 (7)	0.982 (7)	1.016 (6)	1.242 (7)
(0°/90°/0°)		1.039 (12)	1.907 (12)	0.952 (11)	1.472 (11)	1.028 (8)	1.479 (10)	0.970 (13)	2.141 (15)	
(90°/0°/90°)		1.809 (5)	2.526 (4)	1.501 (6)	1.934 (5)	1.446 (6)	1.782 (5)	1.982 (5)	3.220 (4)	
(0°/90°/0°/90°)		1.903 (8)	3.298 (6)	1.445 (8)	2.248 (8)	1.551 (7)	2.127 (7)	1.831 (8)	3.228 (6)	
(0°/90°/90°/0°)		1.468 (10)	2.744 (10)	1.277 (8)	1.912 (8)	1.378 (8)	1.962 (8)	1.344 (11)	3.190 (11)	
(90°/0°/0°/90°)		2.050 (6)	3.160 (4)	1.579 (6)	2.125 (5)	1.600 (6)	2.071 (6)	2.215 (6)	3.766 (4)	
0.75		(0°)	0.422 (10)	0.578 (11)	0.404 (9)	0.512 (10)	0.339 (9)	0.403 (9)	0.503 (10)	0.784 (11)
		(0°/90°)	0.623 (5)	0.692 (5)	0.473 (6)	0.533 (6)	0.478 (5)	0.512 (5)	0.578 (5)	0.633 (5)
	(0°/90°/0°)	0.612 (8)	0.857 (8)	0.567 (9)	0.678 (7)	0.573 (6)	0.678 (7)	0.588 (8)	0.956 (10)	
	(90°/0°/90°)	1.282 (4)	1.652 (3)	0.990 (4)	1.175 (4)	0.902 (4)	1.054 (4)	1.497 (4)	2.075 (3)	
	(0°/90°/0°/90°)	1.233 (5)	1.586 (5)	0.898 (6)	1.066 (6)	0.870 (5)	1.040 (5)	1.111 (5)	1.558 (5)	
	(0°/90°/90°/0°)	0.902 (7)	1.244 (7)	0.738 (6)	0.902 (6)	0.750 (6)	0.935 (5)	0.862 (8)	1.424 (8)	
	(90°/0°/0°/90°)	1.383 (4)	1.794 (4)	1.010 (5)	1.154 (4)	0.947 (5)	1.082 (4)	1.591 (4)	2.248 (3)	
	1.0	(0°)	0.272 (8)	0.329 (8)	0.258 (7)	0.298 (7)	0.212 (7)	0.234 (7)	0.335 (8)	0.446 (8)
		(0°/90°)	0.435 (4)	0.469 (4)	0.307 (5)	0.342 (5)	0.335 (5)	0.366 (4)	0.401 (5)	0.438 (4)
(0°/90°/0°)		0.370 (7)	0.496 (6)	0.349 (6)	0.403 (6)	0.369 (6)	0.413 (5)	0.422 (6)	0.548 (7)	
(90°/0°/90°)		1.044 (3)	1.228 (3)	0.778 (4)	0.922 (3)	0.734 (4)	0.849 (4)	1.252 (3)	1.651 (3)	
(0°/90°/0°/90°)		0.828 (4)	0.998 (4)	0.566 (4)	0.670 (5)	0.624 (4)	0.678 (4)	0.805 (4)	0.984 (4)	
(0°/90°/90°/0°)		0.599 (6)	0.728 (5)	0.482 (5)	0.565 (5)	0.525 (5)	0.596 (4)	0.600 (6)	0.816 (6)	
(90°/0°/0°/90°)		1.071 (3)	1.243 (3)	0.712 (4)	0.839 (4)	0.674 (4)	0.760 (4)	1.300 (3)	1.671 (3)	

**Table 7**

Distribution of ND-LCP and circumferential wave numbers of single-layer and multilayer cylindrical shells consisting of FG-NCLs according to  $R/h$  with different  $T$ .

$R/h$	Number and arrangement of layers	$P_{1st}^{Lcr} \times 100, (n_{cr}), T = 300 \text{ (K)}$							
		$U$		$V$		$\diamond$		$X$	
		SDT	KLT	SDT	KLT	SDT	KLT	SDT	KLT
25	(0°/90°)	0.629 (7)	0.732 (7)	0.506 (9)	0.588 (8)	0.480 (8)	0.527 (7)	0.564 (7)	0.661 (7)
	(0°/90°/0°)	0.601 (11)	0.998 (13)	0.574 (10)	0.772 (11)	0.618 (11)	0.779 (10)	0.616 (12)	1.117 (15)
	(90°/0°/90°)	1.142 (5)	1.445 (4)	0.911 (5)	1.072 (5)	0.877 (5)	0.986 (5)	1.299 (5)	1.816 (4)
	(0°/90°/90°/0°)	0.889 (10)	1.446 (10)	0.770 (9)	1.014 (8)	0.855 (7)	1.039 (8)	0.866 (11)	1.672 (12)
30	(0°/90°)	0.389 (8)	0.433 (7)	0.310 (8)	0.346 (8)	0.298 (7)	0.315 (7)	0.356 (6)	0.392 (7)
	(0°/90°/0°)	0.420 (12)	0.579 (13)	0.372 (10)	0.450 (11)	0.460 (6)	0.460 (11)	0.387 (12)	0.647 (15)
	(90°/0°/90°)	0.752 (5)	0.923 (4)	0.586 (6)	0.662 (5)	0.554 (6)	0.609 (5)	0.881 (5)	1.143 (4)
	(0°/90°/90°/0°)	0.600 (11)	0.839 (10)	0.482 (9)	0.594 (9)	0.472 (7)	0.607 (8)	0.581 (11)	0.969 (12)
40	(0°/90°)	0.188 (8)	0.193 (7)	0.132 (8)	0.150 (9)	0.134 (8)	0.143 (8)	0.156 (6)	0.176 (7)
	(0°/90°/0°)	0.197 (14)	0.245 (13)	0.165 (10)	0.192 (11)	0.172 (10)	0.194 (10)	0.198 (14)	0.274 (15)
	(90°/0°/90°)	0.383 (5)	0.434 (5)	0.284 (6)	0.324 (5)	0.258 (6)	0.291 (6)	0.466 (5)	0.581 (4)
	(0°/90°/90°/0°)	0.264 (8)	0.357 (10)	0.217 (9)	0.256 (9)	0.229 (8)	0.262 (8)	0.246 (9)	0.410 (12)
50	(0°/90°)	0.098 (8)	0.105 (8)	0.070 (9)	0.079 (9)	0.074 (8)	0.077 (8)	0.091 (8)	0.095 (8)
	(0°/90°/0°)	0.099 (12)	0.126 (13)	0.083 (10)	0.099 (11)	0.911 (12)	0.101 (11)	0.112 (11)	0.140 (15)
	(90°/0°/90°)	0.233 (6)	0.248 (5)	0.169 (6)	0.180 (6)	0.155 (6)	0.162 (6)	0.281 (5)	0.325 (5)
	(0°/90°/90°/0°)	0.140 (9)	0.184 (10)	0.114 (9)	0.135 (9)	0.124 (8)	0.138 (8)	0.153 (13)	0.211 (12)
$T = 500 \text{ (K)}$									
25	(0°/90°)	0.654 (7)	0.723 (7)	0.489 (8)	0.581 (8)	0.484 (7)	0.520 (7)	0.565 (7)	0.654 (7)
	(0°/90°/0°)	0.609 (10)	0.984 (13)	0.573 (11)	0.762 (11)	0.609 (10)	0.766 (10)	0.606 (13)	1.103 (15)
	(90°/0°/90°)	1.134 (5)	1.426 (4)	0.896 (5)	1.057 (5)	0.861 (5)	0.973 (5)	1.291 (5)	1.790 (4)
	(0°/90°/90°/0°)	0.909 (10)	1.421 (10)	0.771 (9)	0.998 (8)	0.835 (8)	1.022 (8)	0.878 (9)	1.646 (12)
30	(0°/90°)	0.377 (7)	0.428 (7)	0.304 (9)	0.342 (8)	0.297 (8)	0.311 (7)	0.352 (7)	0.388 (7)
	(0°/90°/0°)	0.386 (13)	0.570 (13)	0.347 (11)	0.443 (11)	0.367 (9)	0.446 (10)	0.400 (13)	0.641 (14)
	(90°/0°/90°)	0.733 (5)	0.913 (4)	0.577 (5)	0.654 (5)	0.540 (6)	0.600 (5)	0.881 (5)	1.128 (4)
	(0°/90°/90°/0°)	0.604 (9)	0.824 (10)	0.474 (9)	0.584 (9)	0.506 (8)	0.596 (8)	0.570 (13)	0.953 (12)
40	(0°/90°)	0.159 (7)	0.191 (7)	0.145 (7)	0.148 (9)	0.133 (8)	0.141 (8)	0.171 (8)	0.174 (7)
	(0°/90°/0°)	0.186 (15)	0.241 (13)	0.158 (12)	0.189 (11)	0.154 (8)	0.191 (10)	0.191 (13)	0.270 (15)
	(90°/0°/90°)	0.373 (5)	0.428 (5)	0.282 (6)	0.319 (6)	0.258 (6)	0.287 (6)	0.463 (5)	0.574 (5)
	(0°/90°/90°/0°)	0.284 (7)	0.350 (10)	0.221 (9)	0.252 (9)	0.226 (7)	0.258 (8)	0.285 (9)	0.403 (12)
50	(0°/90°)	0.098 (7)	0.104 (8)	0.068 (10)	0.081 (10)	0.067 (8)	0.076 (8)	0.085 (7)	0.095 (8)
	(0°/90°/0°)	0.099 (11)	0.124 (13)	0.090 (10)	0.101 (10)	0.801 (8)	0.099 (11)	0.106 (13)	0.139 (15)
	(90°/0°/90°)	0.227 (6)	0.245 (5)	0.167 (6)	0.178 (6)	0.150 (6)	0.160 (6)	0.274 (5)	0.320 (5)
	(0°/90°/90°/0°)	0.152 (10)	0.191 (10)	0.104 (9)	0.133 (9)	0.116 (9)	0.136 (8)	0.160 (13)	0.207 (12)
$T = 700 \text{ (K)}$									
25	(0°/90°)	0.633 (7)	0.718 (7)	0.489 (8)	0.578 (8)	0.467 (7)	0.516 (7)	0.587 (6)	0.650 (7)
	(0°/90°/0°)	0.616 (12)	0.977 (13)	0.573 (11)	0.757 (11)	0.589 (10)	0.761 (10)	0.595 (13)	1.096 (15)
	(90°/0°/90°)	1.118 (5)	1.418 (4)	0.895 (5)	1.050 (5)	0.850 (6)	0.966 (5)	1.283 (5)	1.780 (4)
	(0°/90°/90°/0°)	0.853 (9)	1.408 (10)	0.761 (10)	0.991 (8)	0.829 (9)	1.013 (8)	0.879 (12)	1.630 (12)
30	(0°/90°)	0.390 (8)	0.425 (7)	0.301 (9)	0.340 (8)	0.290 (8)	0.309 (7)	0.356 (7)	0.386 (7)
	(0°/90°/0°)	0.400 (13)	0.566 (13)	0.366 (11)	0.440 (11)	0.344 (10)	0.442 (10)	0.386 (13)	0.635 (15)
	(90°/0°/90°)	0.742 (5)	0.907 (4)	0.577 (5)	0.650 (5)	0.527 (6)	0.596 (5)	0.871 (5)	1.121 (4)
	(0°/90°/90°/0°)	0.559 (10)	0.817 (10)	0.473 (9)	0.580 (9)	0.486 (9)	0.591 (8)	0.561 (11)	0.945 (12)
40	(0°/90°)	0.177 (8)	0.190 (7)	0.126 (9)	0.148 (9)	0.128 (8)	0.140 (8)	0.161 (8)	0.174 (7)
	(0°/90°/0°)	0.180 (12)	0.239 (13)	0.154 (11)	0.188 (11)	0.171 (9)	0.189 (10)	0.203 (12)	0.269 (15)
	(90°/0°/90°)	0.373 (5)	0.425 (5)	0.280 (6)	0.317 (6)	0.258 (6)	0.285 (6)	0.455 (5)	0.569 (5)
	(0°/90°/90°/0°)	0.264 (8)	0.347 (10)	0.222 (8)	0.251 (9)	0.226 (9)	0.256 (8)	0.292 (12)	0.400 (13)
50	(0°/90°)	0.098 (7)	0.103 (8)	0.065 (9)	0.078 (9)	0.071 (9)	0.076 (8)	0.087 (8)	0.094 (8)
	(0°/90°/0°)	0.111 (15)	0.123 (13)	0.080 (11)	0.098 (11)	0.085 (10)	0.098 (10)	0.113 (10)	0.138 (15)
	(90°/0°/90°)	0.226 (5)	0.243 (5)	0.165 (6)	0.177 (6)	0.157 (7)	0.159 (6)	0.277 (5)	0.318 (5)
	(0°/90°/90°/0°)	0.145 (9)	0.179 (10)	0.110 (9)	0.132 (9)	0.111 (8)	0.137 (9)	0.142 (11)	0.206 (12)

for  $T = 700 \text{ (K)}$ , those effects occur in shells consisting of inverted pyramid and rhombic prism originating layers (See, Figs. 4–9).

For all  $T$  and when the  $R/h$  ratio increases from 25 to 50, the most pronounced shear strains effects on the ND-LCP of multilayer shells occur in shells with different arrays and number of layers composed of layers originating from sandglass. For instance, at  $T = 300, 500$  and  $700 \text{ (K)}$ , the most prominent transverse shear strain effects occur in the four-layer cylindrical shells with (0°/90°/90°/0°)-arrangement for  $R/h=25$  (see, Table 7). In the SDT framework, the influences of temperature rise on the  $P_{1st}^{Lcr}$  generally increase irregularly as  $R/h$  increment. At  $T = 500 \text{ (K)}$ , the most prominent influence of temperature rise on the ND-LCP occurs in the sandglass originating (0°/90°/90°/0°)-sequence shell, while at  $T = 700 \text{ (K)}$ , those influences on the  $P_{1st}^{Lcr}$  occurs in the (0°/90°)-alignment shell with U-pattern for  $R/h = 50$  (see, Table 7).

### 5. Conclusions

The multilayer cylindrical shells formed from nanocomposite layers made of CWCNT reinforced polymers are assumed to have four types of profiles based on uniform and linear distributions of mechanical properties. This study highlights the influences of geometric parameters, transverse shear stresses, CNT-patterns in the layers and temperature rise on the stability performance of multilayer cylindrical shells consisting of FG-NCLs under the lateral pressure within SDT and KLT. These findings provide useful information for designing multilayer cylindrical shells composed of FG-CNT patterned layers to optimize stability under lateral pressure.

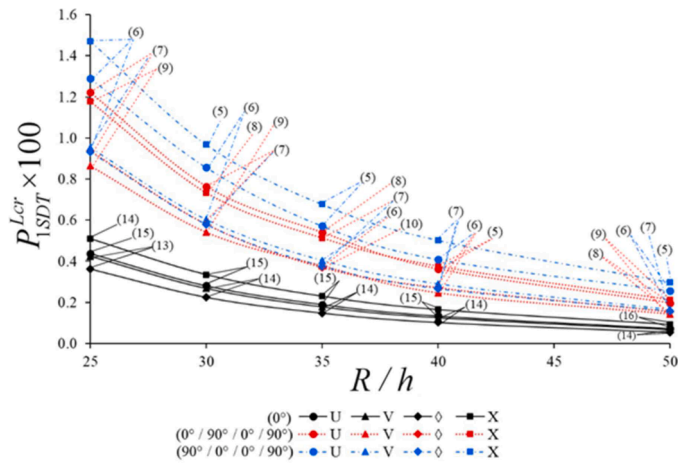


Fig. 4. Distribution of ND-LCP and circumferential wave numbers of  $(0^\circ)$  single-layer and,  $(0^\circ/90^\circ/0^\circ/90^\circ)$  and  $(90^\circ/0^\circ/0^\circ/90^\circ)$ -sequence cylindrical shells consisting of uniform and FG-NCLs within SDT according to  $R/h$  for  $T = 300$  (K).

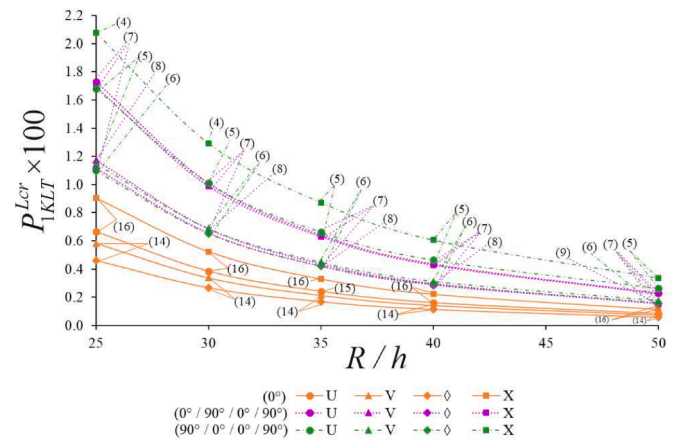


Fig. 7. Distribution of ND-LCP and circumferential wave numbers of  $(0^\circ)$  single-layer and,  $(0^\circ/90^\circ/0^\circ/90^\circ)$  and  $(90^\circ/0^\circ/0^\circ/90^\circ)$ -sequence cylindrical shells consisting of uniform and FG-NCLs within KLT according to  $R/h$  for  $T = 500$  (K).

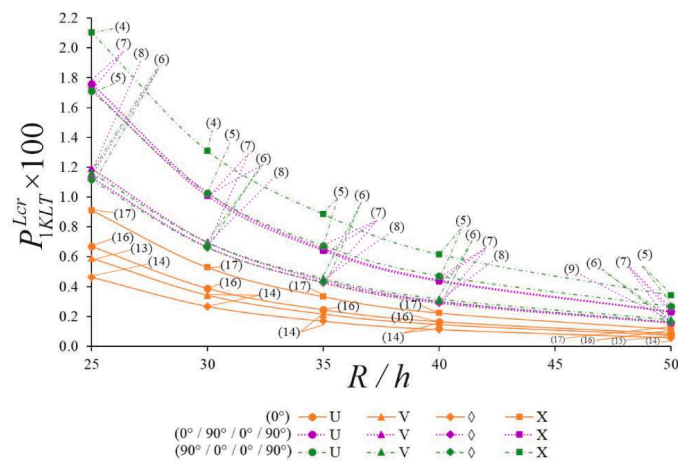


Fig. 5. Distribution of ND-LCP and circumferential wave numbers of  $(0^\circ)$  single-layer and,  $(0^\circ/90^\circ/0^\circ/90^\circ)$  and  $(90^\circ/0^\circ/0^\circ/90^\circ)$ -sequence cylindrical shells consisting of uniform and FG-NCLs within KLT according to  $R/h$  for  $T = 300$  (K).

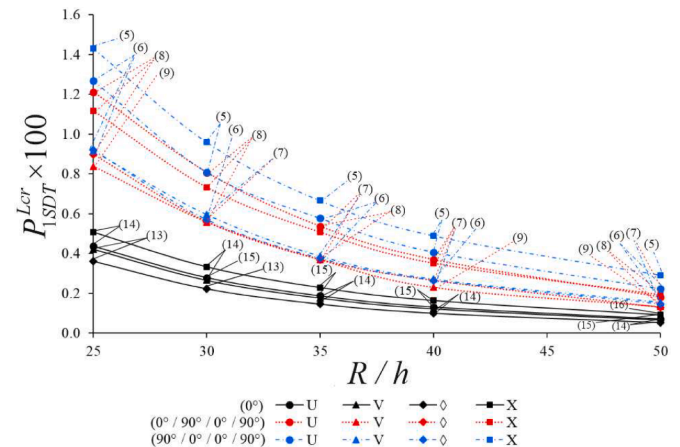


Fig. 8. Distribution of ND-LCP and circumferential wave numbers of  $(0^\circ)$  single-layer and,  $(0^\circ/90^\circ/0^\circ/90^\circ)$  and  $(90^\circ/0^\circ/0^\circ/90^\circ)$ -sequence cylindrical shells consisting of uniform and FG-NCLs within SDT according to  $R/h$  for  $T = 700$  (K).

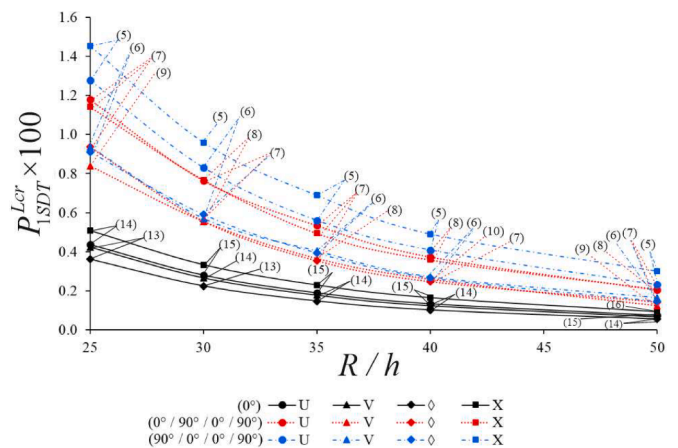


Fig. 6. Distribution of ND-LCP and circumferential wave numbers of  $(0^\circ)$  single-layer and,  $(0^\circ/90^\circ/0^\circ/90^\circ)$  and  $(90^\circ/0^\circ/0^\circ/90^\circ)$ -sequence cylindrical shells consisting of uniform and FG-NCLs within SDT according to  $R/h$  for  $T = 500$  (K).

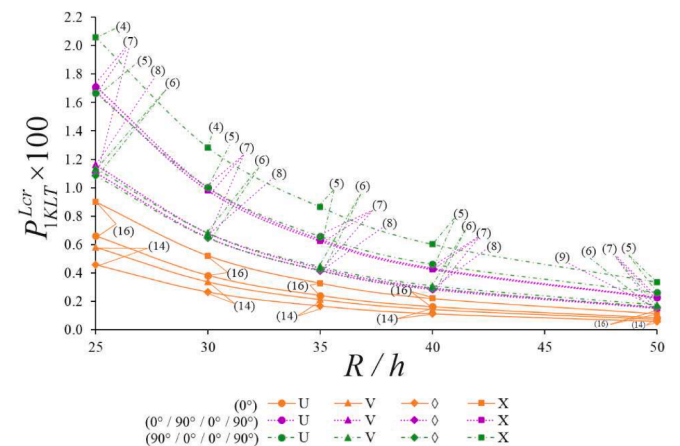


Fig. 9. Distribution of ND-LCP and circumferential wave numbers of  $(0^\circ)$  single-layer and,  $(0^\circ/90^\circ/0^\circ/90^\circ)$  and  $(90^\circ/0^\circ/0^\circ/90^\circ)$ -sequence cylindrical shells consisting of uniform and FG-NCLs within KLT according to  $R/h$  for  $T = 700$  (K).

**Funding**

This article received no funding support.

**Institutional review board statement**

Not applicable.

**Informed consent statement**

Not applicable.

**CRedit authorship contribution statement**

**M. Avey:** Conceptualization, Methodology, Software, Validation,

Formal analysis, Investigation, Resources, Writing – original draft. **N. Fantuzzi:** Software, Validation, Writing – review & editing. **A.H. Sofiyev:** Validation, Writing – review & editing. **A.D. Zamanov:** Validation. **Y.N. Hasanov:** Validation. **E. Schnack:** Writing – review & editing.

**Declaration of Competing Interest**

The authors declare no potential conflicts of interest with respect to the research, authorship and publication of this article.

**Data availability**

No data were reported in this study.  
No data was used for the research described in the article.

**Appendix A**

Here  $L_{p_1q_1}$  ( $p_1, q_1 = 1, 2, \dots, 4$ ) are differential operators and are defined as:

$$\begin{aligned}
 L_{11} &= h \frac{\partial^2}{\partial x^2} \left[ (H_{11} - H_{31}) \frac{\partial^2}{\partial y^2} + H_{12} \frac{\partial^2}{\partial x^2} \right], \quad L_{12} = -\frac{\partial^2}{\partial x^2} \left[ H_{13} \frac{\partial^2}{\partial x^2} + (H_{14} + H_{32}) \frac{\partial^2}{\partial y^2} \right], \\
 L_{13} &= \frac{\partial}{\partial x} \left[ H_{15} \frac{\partial^2}{\partial x^2} + H_{35} \frac{\partial^2}{\partial y^2} - \Pi_3 \right], \quad L_{14} = (H_{18} + H_{38}) \frac{\partial^3}{\partial x^2 \partial y} \\
 L_{21} &= h \frac{\partial^2}{\partial y^2} \left[ H_{21} \frac{\partial^2}{\partial y^2} + (H_{22} - H_{31}) \frac{\partial^2}{\partial x^2} \right], \quad L_{22} = -\frac{\partial^2}{\partial y^2} \left[ (H_{32} + H_{23}) \frac{\partial^2}{\partial x^2} + H_{24} \frac{\partial^2}{\partial y^2} \right], \\
 L_{23} &= (H_{35} + H_{25}) \frac{\partial^3}{\partial x \partial y^2}, \quad L_{24} = \frac{\partial}{\partial y} \left( H_{38} \frac{\partial^2}{\partial x^2} + H_{28} \frac{\partial^2}{\partial y^2} - \Pi_4 \right) \\
 L_{31} &= h \left[ S_{11} \frac{\partial^4}{\partial y^4} + (S_{12} + S_{21} + S_{31}) \frac{\partial^4}{\partial x^2 \partial y^2} + S_{22} \frac{\partial^4}{\partial x^4} \right] \\
 L_{32} &= \frac{1}{R} \frac{\partial^2}{\partial x^2} - S_{23} \frac{\partial^4}{\partial x^4} - (S_{24} + S_{13} - S_{32}) \frac{\partial^4}{\partial x^2 \partial y^2} - S_{14} \frac{\partial^4}{\partial y^4} \\
 L_{33} &= \frac{\partial}{\partial x} \left[ S_{25} \frac{\partial^2}{\partial x^2} + (S_{15} + S_{35}) \frac{\partial^2}{\partial y^2} \right], \quad L_{34} = \frac{\partial}{\partial y} \left[ (S_{28} + S_{38}) \frac{\partial^2}{\partial x^2} + S_{18} \frac{\partial^2}{\partial y^2} \right] \\
 L_{41} &= \frac{h}{R} \frac{\partial^2}{\partial x^2}, \quad L_{42} = -\frac{\partial^2}{\partial y^2}, \quad L_{43} = \Pi_3 \frac{\partial}{\partial x}, \quad L_{44} = \Pi_4 \frac{\partial}{\partial y}.
 \end{aligned}
 \tag{A1}$$

where  $\Pi_3 = \Pi_4 = \sum_{i=1}^N [f^{(i)}(z_i) - f^{(i)}(z_{i-1})]$  and the following definitions apply:

$$\begin{aligned}
 H_{11} &= A_{11}^1 S_{11} + A_{12}^1 S_{21}, \quad H_{12} = A_{11}^1 S_{12} + A_{12}^1 S_{22}, \quad H_{13} = A_{11}^1 S_{13} + A_{12}^1 S_{23} + A_{11}^2, \quad H_{14} = A_{11}^1 S_{14} + A_{12}^1 S_{24} + H_{12}^2, \\
 H_{15} &= A_{11}^1 S_{15} + A_{12}^1 S_{25} + A_{15}^1, \quad H_{18} = A_{11}^1 S_{18} + A_{12}^1 S_{28} + A_{18}^1, \quad H_{21} = A_{21}^1 S_{11} + A_{22}^1 S_{21}, \quad H_{22} = A_{21}^1 S_{12} + A_{22}^1 S_{22}, \\
 H_{23} &= A_{21}^1 S_{13} + A_{22}^1 S_{23} + A_{21}^2, \quad H_{24} = A_{21}^1 S_{14} + A_{22}^1 S_{24} + A_{22}^2, \quad H_{25} = A_{21}^1 S_{15} + A_{22}^1 S_{25} + A_{25}^1, \\
 H_{28} &= A_{21}^1 S_{18} + A_{22}^1 S_{28} + A_{28}^1, \quad H_{31} = A_{66}^1 S_{31}, \quad H_{32} = A_{66}^1 S_{32} + 2A_{66}^2, \quad H_{35} = A_{35}^1 - A_{66}^1 S_{35}, \quad H_{38} = A_{38}^1 - A_{66}^1 S_{38}, \\
 S_{11} &= \frac{A_{22}^0}{\Delta}, \quad S_{12} = -\frac{A_{12}^0}{\Delta}, \quad S_{13} = \frac{A_{12}^0 A_{21}^1 - A_{11}^1 A_{22}^0}{\Delta}, \quad S_{14} = \frac{A_{12}^0 A_{22}^1 - A_{12}^1 A_{22}^0}{\Delta}, \quad S_{15} = \frac{A_{25}^0 A_{12}^0 - A_{15}^0 A_{22}^0}{\Delta}, \\
 S_{18} &= \frac{A_{28}^0 A_{12}^0 - A_{18}^0 A_{22}^0}{\Delta}, \quad S_{21} = -\frac{A_{21}^0}{\Delta}, \quad S_{22} = \frac{A_{11}^0}{\Delta}, \quad S_{23} = \frac{A_{11}^1 A_{21}^0 - A_{21}^1 A_{11}^0}{\Delta}, \quad S_{24} = \frac{A_{12}^1 A_{21}^0 - A_{22}^1 A_{11}^0}{\Delta}, \\
 S_{25} &= \frac{A_{15}^0 A_{21}^0 - A_{25}^0 A_{11}^0}{\Delta}, \quad S_{28} = \frac{A_{18}^0 A_{21}^0 - A_{28}^0 A_{11}^0}{\Delta}, \quad S_{31} = \frac{1}{A_{66}^0}, \quad S_{32} = -\frac{2A_{66}^1}{A_{66}^0}, \quad S_{35} = \frac{A_{35}^0}{A_{66}^0}, \quad S_{38} = \frac{A_{38}^0}{A_{66}^0}, \\
 \Delta &= A_{11}^0 A_{22}^0 - A_{12}^0 A_{21}^0.
 \end{aligned}
 \tag{A2}$$

in which

$$\begin{aligned}
A_{11}^{k_1} &= \sum_{i=1}^N \int_{z_{i-1}}^{z_i} K_{11}^{(i)} z^{k_1} dz, A_{12}^{k_1} = \sum_{i=1}^N \int_{z_{i-1}}^{z_i} K_{12}^{(i)} z^{k_1} dz = \sum_{i=1}^N \int_{z_{i-1}}^{z_i} K_{21}^{(i)} z^{k_1} dz = A_{21}^{k_1}, A_{22}^{k_1} = \sum_{i=1}^N \int_{z_{i-1}}^{z_i} K_{22}^{(i)} z^{k_1} dz, \\
A_{66}^{k_1} &= \sum_{i=1}^N \int_{z_{i-1}}^{z_i} K_{66}^{(i)} z^{k_1} dz, A_{15}^{k_2} = \sum_{i=1}^N \int_{z_{i-1}}^{z_i} K_{11}^{(i)} \Pi_{1(z,T)}^{(i)} z^{k_2} dz, A_{18}^{k_2} = \sum_{i=1}^N \int_{z_{i-1}}^{z_i} K_{12}^{(i)} \Pi_{2(z,T)}^{(i)} z^{k_2} dz, \\
A_{25}^{k_2} &= \sum_{i=1}^N \int_{z_{i-1}}^{z_i} K_{21}^{(i)} \Pi_{1(z,T)}^{(i)} z^{k_2} dz, A_{28}^{k_2} = \sum_{i=1}^N \int_{z_{i-1}}^{z_i} K_{22}^{(i)} \Pi_{2(z,T)}^{(i)} z^{k_2} dz, A_{35}^{k_2} = \sum_{i=1}^N \int_{z_{i-1}}^{z_i} K_{66}^{(i)} \Pi_{1(z,T)}^{(i)} z^{k_2} dz, \\
A_{38}^{k_2} &= \sum_{i=1}^N \int_{z_{i-1}}^{z_i} K_{66}^{(i)} \Pi_{2(z,T)}^{(i)} z^{k_2} dz, k_1 = 0, 1, 2; k_2 = 0, 1.
\end{aligned} \tag{A3}$$

## Appendix B

$F_{p_1 q_1}$  ( $i, j = 1, 2, 3, 4$ ) are given by,

$$\begin{aligned}
F_{11} &= h \left[ (H_{11} - H_{31}) \left( \frac{n}{R} \right)^2 + H_{12} \left( \frac{m\pi}{L} \right)^2 \right] \left( \frac{m\pi}{L} \right)^2, F_{12} = \left[ (H_{14} + H_{32}) \left( \frac{n}{R} \right)^2 + H_{13} \left( \frac{m\pi}{L} \right)^2 \right] \left( \frac{m\pi}{L} \right)^2, \\
F_{13} &= \left[ H_{15} \left( \frac{m\pi}{L} \right)^2 + H_{35} \left( \frac{n}{R} \right)^2 + \Pi_3 \right] \frac{m\pi}{a}, F_{14} = (H_{18} + H_{38}) \frac{n}{R} \left( \frac{m\pi}{L} \right)^2, \\
F_{21} &= h \left[ H_{21} \left( \frac{n}{R} \right)^2 + (H_{22} - H_{31}) \left( \frac{m\pi}{L} \right)^2 \right] \left( \frac{n}{R} \right)^2, F_{22} = \left[ (H_{32} + H_{23}) \left( \frac{m\pi}{L} \right)^2 + H_{24} \left( \frac{n}{R} \right)^2 \right] \left( \frac{n}{R} \right)^2, \\
F_{23} &= (H_{25} + H_{35}) \left( \frac{m\pi}{L} \right) \left( \frac{n}{R} \right)^2, F_{24} = \left[ H_{28} \left( \frac{n}{R} \right)^2 + H_{38} \left( \frac{m\pi}{L} \right)^2 + \Pi_4 \right] \frac{n}{R}, \\
F_{31} &= h \left[ S_{22} \left( \frac{m\pi}{L} \right)^4 + (S_{12} + S_{21} + S_{31}) \left( \frac{m\pi}{LR} \right)^2 + S_{11} \left( \frac{n}{R} \right)^4 \right], \\
F_{32} &= S_{23} \left( \frac{m\pi}{L} \right)^4 + (S_{24} + S_{13} + S_{32}) \left( \frac{m\pi}{LR} \right)^2 + S_{14} \left( \frac{n}{R} \right)^4 + \frac{1}{R} \left( \frac{m\pi}{L} \right)^2, \\
F_{33} &= \left[ S_{25} \left( \frac{m\pi}{L} \right)^2 + (S_{15} + S_{35}) \left( \frac{n}{R} \right)^2 \right] \frac{m\pi}{L}, F_{34} = \left[ (S_{28} + S_{38}) \left( \frac{m\pi}{L} \right)^2 + S_{18} \left( \frac{n}{R} \right)^2 \right] \frac{n}{R}, \\
F_{41} &= \frac{h}{R} \left( \frac{m\pi}{L} \right)^2, F_{42} = \left( \frac{n}{R} \right)^2, F_{43} = \Pi_3 \frac{m\pi}{L}, F_{44} = \Pi_4 \frac{n}{R}
\end{aligned} \tag{B1}$$

## References

- [1] S. Iijima, T. Ichihashi, Single-shell carbon nanotubes of 1-nm diameter, *Nature* 363 (1993) 603–604, <https://doi.org/10.1038/363603a0>.
- [2] K. Suzuki, S. Nomura, On elastic properties of single-walled carbon nanotubes as composite reinforcing fillers, *J. Compos. Mater.* 41 (9) (2007) 1123–1135, <https://doi.org/10.1177/0021998306067298>.
- [3] T.W. Ebbesen, *Carbon Nanotubes: Preparation and Properties*, CRC press, 1996.
- [4] A. Garg, H.D. Chalak, M.Q. Belarbi, A.M. Zenkour, R. Sahoo, Estimation of carbon nanotubes and their applications as reinforcing composite materials—an engineering review, *Compos. Struct.* 272 (2021), 114234, <https://doi.org/10.1016/j.compstruct.2021.114234>.
- [5] K.I. Winey, R.A. Vaia, Polymer nanocomposites, *MRS Bull.* 32 (4) (2011) 314–322, <https://doi.org/10.1557/mrs2007.229>.
- [6] M.A.L. Manchado, L. Valentini, J. Biagiotti, J.M. Kenny, Thermal and mechanical properties of single-walled carbon nanotubes–polypropylene composites prepared by melt processing, *Carbon N Y* 43 (2005) 1499–1505, <https://doi.org/10.1016/j.carbon.2005.01.031>.
- [7] N.K. Votarikari, S.K. Gugulothu, Influence of nanofluid in thermal and mechanical properties of NR alumina polymer nanocomposites, *J. Compos. Part C 4* (2021), 100094, <https://doi.org/10.1016/j.jcomc.2023.100361>.
- [8] T. Mishra, P. Mandal, A.K. Rout, D.A. Sahoo, State-of-the-art review on potential applications of natural fiber-reinforced polymer composite filled with inorganic nanoparticle, *J. Compos. Part C 9* (2022), 100298, <https://doi.org/10.1016/j.jcomc.2022.100298>.
- [9] Y. Han, J. Elliott, Molecular dynamics simulations of the elastic properties of polymer/carbon nanotube composites, *Comput. Mater. Sci.* 39 (2007) 315–323, <https://doi.org/10.1016/j.commatsci.2006.06.011>.
- [10] H.-S. Shen, Nonlinear bending of functionally graded carbon nanotube-reinforced composite plates in thermal environments, *Compos. Struct.* 91 (2009) 9–19, <https://doi.org/10.1016/j.compstruct.2009.04.026>.
- [11] H.-S. Shen, Postbuckling of nanotube-reinforced composite cylindrical shells in thermal environments, part II: pressure-loaded shells, *Compos. Struct.* 93 (2011) 2496–2503, <https://doi.org/10.1016/j.compositesb.2013.04.034>.
- [12] H.-S. Shen, Postbuckling of nanotube-reinforced composite cylindrical panels resting on elastic foundations subjected to lateral pressure in thermal environments, *Eng. Struct.* 122 (2016) 174–183, <https://doi.org/10.1016/j.engstruct.2016.05.004>.
- [13] S. Chakraborty, T. Dey, R. Kumar, Stability and vibration analysis of CNT-reinforced functionally graded laminated composite cylindrical shell panels using semi-analytical approach, *Compos. Part B Eng.* 168 (2019) 1–14, <https://doi.org/10.1016/j.compositesb.2018.12.051>.
- [14] P.T. Hieu, H.V. Tung, Postbuckling behavior of CNT-reinforced composite cylindrical shell surrounded by an elastic medium and subjected to combined mechanical loads in thermal environments, *J. Thermoplast. Compos. Mater.* 32 (10) (2019) 1319–1346, <https://doi.org/10.1177/0892705718796551>.
- [15] P.T. Hieu, H.V. Tung, Thermomechanical postbuckling of pressure-loaded CNT-reinforced composite cylindrical shells under tangential edge constraints and various temperature conditions, *Polym. Compos.* 41 (1) (2020) 244–257, <https://doi.org/10.1002/pc.25365>.
- [16] A.R. Ghasemi, M. Soleymani, A new efficient buckling investigation of functionally graded CNT/fiber/polymer/metal composite panels exposed to hydrostatic pressure considering simultaneous manufacturing-induced agglomeration and imperfection issues, *Euro. Phys. J. Plus* 136 (12) (2021) 1220, <https://doi.org/10.1140/epjp/s13360-021-02197-y>.
- [17] M. Nejati, R. Dimitri, R. Tornabene, M.H. Yas, Thermal buckling of nanocomposite stiffened cylindrical shells reinforced by functionally graded wavy carbon nanotubes with temperature-dependent properties, *Appl. Sci.* 7 (12) (2017) 1223, <https://doi.org/10.3390/app7121223>.
- [18] M. Baccocchi, Buckling analysis of three-phase CNT/polymer/fiber functionally graded orthotropic plates: influence of the non-uniform distribution of the oriented fibers on the critical load, *Eng. Struct.* 223 (2020), 111176, <https://doi.org/10.1016/j.engstruct.2020.111176>.

- [19] E. Sobhani, A.M. Masoodi, A comprehensive shell approach for vibration of porous nano-enriched polymer composite coupled spheroidal-cylindrical shells, *Compos. Struct.* 289 (2022), 115464, <https://doi.org/10.1016/j.compstruct.2022.115464>.
- [20] A. Muc, S. Kubis, L. Bratek, M. Muc-Wierzgoń, Higher order theories for the buckling and post-buckling studies of shallow spherical shells made of functionally graded materials, *Compos. Struct.* 295 (2022), 115851, <https://doi.org/10.1016/j.compstruct.2022.115851>.
- [21] X. Shi, P. Zuo, R. Zhong, C.C. Guo, Q. Wang, Vibration analysis of combined functionally graded cylindrical-conical shells coupled with annular plates in thermal environment, *Compos. Struct.* 294 (2022), 115738, <https://doi.org/10.1016/j.compstruct.2022.115738>.
- [22] M. Avey, N. Fantuzzi, A.H. Sofiyev, Thermoelastic stability of CNT patterned conical shells under thermal loading in the framework of shear deformation theory, *Mech. Adv. Mater. Struct.* 30 (9) (2023) 1828–1841, <https://doi.org/10.1080/15376494.2022.2045653>.
- [23] A.H. Sofiyev, N. Fantuzzi, Stability analysis of shear deformable inhomogeneous nanocomposite cylindrical shells under hydrostatic pressure in thermal environment, *Materials (Basel)* 16 (13) (2023) 4887, <https://doi.org/10.3390/ma16134887>.
- [24] C. Ipek, A.H. Sofiyev, N. Fantuzzi, S.P. Efyendiyeva, Buckling behavior of nanocomposite plates with functionally graded properties under compressive loads in elastic and thermal environments, *J. Appl. Comput. Mech.* 9 (4) (2023) 974–986, <https://doi.org/10.22055/jacm.2023.43091.4019>.
- [25] V.M. Kuriakose, V.M. Sreehari, Vibration and flutter analysis of damaged composite plates under thermal environment and its passive control using piezoelectric patches, *J. Compos. Part C* 11 (2023), 100361, <https://doi.org/10.1016/j.jcocom.2023.100361>.
- [26] H.-S. Shen, Y. Xiang, Y. Fan, D. Hui, Nonlinear bending analysis of FG-GRC laminated cylindrical panels on elastic foundations in thermal environments, *Compos. Part B Eng.* 141 (2018) 148–157, <https://doi.org/10.1016/j.compositesb.2017.12.048>.
- [27] G.T. Monaco, N. Fantuzzi, F. Fabbrocino, R. Luciano, Hygro-thermal vibrations and buckling of laminated nanoplates via nonlocal strain gradient theory, *Compos. Struct.* 262 (2021), 113337, <https://doi.org/10.1016/j.compstruct.2020.113337>.
- [28] G.T. Monaco, N. Fantuzzi, F. Fabbrocino, R. Luciano, Semi-analytical static analysis of nonlocal strain gradient laminated composite nanoplates in hygrothermal environment, *J. Brazil. Soc. Mech. Sci. Eng.* 43 (2021) 274, <https://doi.org/10.1007/s40430-021-02992-9>.
- [29] A.A. Baghdadorani, Y. Kiani, Free vibration analysis of functionally graded cylindrical shells reinforced with graphene platelets, *Compos. Struct.* 276 (2021), 114546, <https://doi.org/10.1016/j.compstruct.2021.114546>.
- [30] M. Avey, N. Fantuzzi, A.H. Sofiyev, Vibration of laminated functionally graded nanocomposite structures considering the transverse shear stresses and rotary inertia, *Compos. Struct.* 301 (2022), 116209, <https://doi.org/10.1016/j.compstruct.2022.116209>.
- [31] M. Avey, N. Fantuzzi, A.H. Sofiyev, On the solution of thermal buckling problem of moderately thick laminated conical shells containing carbon nanotube originating layers, *Materials (Basel)* 15 (21) (2022) 7427, <https://doi.org/10.3390/ma15217427>.
- [32] H.-S. Shen, C. Li, X.H. Huang, Assessment of negative Poisson's ratio effect on the postbuckling of pressure-loaded FG-CNTRC laminated cylindrical shells, *Mech. Bas. Des. Struct. Mach.* 51 (4) (2023) 1856–1880, <https://doi.org/10.1080/15397734.2021.1880934>.
- [33] X. Chen, H.S. Shen, C. Li, Re-examination for linear and nonlinear free vibration of porous sandwich cylindrical shells reinforced by graphene platelets, *Mech. Adv. Mater. Struct.* (2023), <https://doi.org/10.1016/j.compstruct.2023.117392>. DOI: 10.1080/15376494.2023.2206821.
- [34] P. Shi, J. Xie, X. Li, Multilayer heterostructure inhomogeneous model for pressurized functionally graded annular structures (cylinder/sphere/annulus) with arbitrary elastic property along the radial direction, *Compos. Struct.* 322 (2023), 117425, <https://doi.org/10.1016/j.compstruct.2023.117425>.
- [35] A.S. Volmir, *Stability of elastic systems*, Nauka: Moscow, Russia, 1967.
- [36] S.A. Ambartsumyan, *Theory of Anisotropic Shells*, NASA, 1964. TT F-118.
- [37] J.N. Reddy, *Mechanics of Laminated Composite Plates and Shells, Theory and Analysis*, CRC Press, New York, 2004, <https://doi.org/10.1201/b12409>.
- [38] G.D. Seidel, D.C. Lagoudas, Micromechanical analysis of the effective elastic properties of carbon nanotube reinforced composites, *Mech. Mater.* 38 (2006) 884–907, <https://doi.org/10.1016/j.mechmat.2005.06.029>.
- [39] X. Li, H. Gao, W.A. Scrivens, D. Fei, X. Xu, M.A. Sutton, P. Reynolds, M.L. Myrick, Reinforcing mechanisms of single-walled carbon nanotube-reinforced polymer composites, *J. Nanosci. Nanotechnol.* 7 (2007) 2309–2317, <https://doi.org/10.1166/jnn.2007.410>.
- [40] V. Anumandla, R.F. Gibson, A comprehensive closed form micromechanics model for estimating the elastic modulus of nanotube-reinforced composites, *Compos. A Appl. Sci.* 37 (2006) 2178–2185, <https://doi.org/10.1016/j.compositesa.2005.09.016>.
- [41] A.M.K. Esawi, M.M. Farag, Carbon nanotube reinforced composites: potential and current challenges, *Mater. Des.* 28 (2007) 2394–2401, <https://doi.org/10.1016/j.matdes.2006.09.022>.
- [42] L. Librescu, S.-Y. Oh, O. Song, Thin-walled beams made of functionally graded materials and operating in a high temperature environment: vibration and stability, *J. Therm. Stress.* 28 (2005) 649–712, <https://doi.org/10.1080/01495730590934038>.
- [43] H.-S. Shen, Z.-X. Wang, Assessment of Voigt and Mori-Tanaka models for vibration analysis of functionally graded plates, *Compos. Struct.* 94 (2012) 2197–2208, <https://doi.org/10.1016/j.compstruct.2012.02.018>.
- [44] H.-S. Shen, Nonlinear vibration of shear deformable FGM cylindrical shells surrounded by an elastic medium, *Compos. Struct.* 94 (2012) 1144–1154, <https://doi.org/10.1016/j.compstruct.2011.11.012>.
- [45] C. Li, T.-W. Chou, A structural mechanics approach for the analysis of carbon nanotubes, *Int. J. Solids Struct.* 40 (10) (2003) 2487–2499, [https://doi.org/10.1016/S0020-7683\(03\)00056-8](https://doi.org/10.1016/S0020-7683(03)00056-8).
- [46] P. Zhang, Y. Huang, P.H. Geubelle, P.A. Klein, K.C. Hwang, The elastic modulus of single-wall carbon nanotubes: a continuum analysis incorporating interatomic potentials, *Int. J. Solids Struct.* 39 (2002) 3893–3906, [https://doi.org/10.1016/S0020-7683\(02\)00186-5](https://doi.org/10.1016/S0020-7683(02)00186-5).
- [47] B.I. Yakobson, M.P. Campbell, C.J. Brabec, J. Bernholc, High strain rate fracture and C-chain unraveling in carbon nanotubes, *Computat. Mater. Sci.* 8 (4) (1997) 341–348, [https://doi.org/10.1016/S0927-0256\(97\)00047-5](https://doi.org/10.1016/S0927-0256(97)00047-5).
- [48] T. Belytschko, S.P. Xiao, G.C. Schatz, R.S. Ruoff, Atomistic simulations of nanotube fracture, *Phys. Rev. B* 65 (23) (2002), 235430, <https://doi.org/10.1103/PhysRevB.65.235430>, 1.
- [49] B. Ashrafi, P. Hubert, Modeling the elastic properties of carbon nanotube array/polymer composites, *Compos. Sci. Technol.* 66 (2006) 387–396, <https://doi.org/10.1016/j.compscitech.2005.07.020>.
- [50] Y. Han, J. Elliott, Molecular dynamics simulations of the elastic properties of polymer/carbon nanotube composites, *Comp. Mater. Sci.* 39 (2007) 315–323, <https://doi.org/10.1016/j.commatsci.2006.06.011>.
- [51] A. Al-Ostaz, G. Pal, P.R. Mantena, A. Cheng, Molecular dynamics simulation of SWCNT-polymer nanocomposite and its constituents, *J. Mater. Sci.* 43 (2008) 164–173, <https://doi.org/10.1007/s10853-007-2132-6>.
- [52] Z.M. Li, Z.Q. Lin, Non-linear buckling and postbuckling of shear deformable anisotropic laminated cylindrical shell subjected to varying external pressure loads, *Compos. Struct.* 92 (2010) 553–567, <https://doi.org/10.1016/j.compstruct.2009.08.048>.